Structures 57 (2023) 105270

Contents lists available at ScienceDirect

Structures

journal homepage: www.elsevier.com/locate/structures

Numerical steady-state and transient responses of a SDOF system constrained by two optimally designed bumpers

Giuseppe Perna *, Maurizio De Angelis, Ugo Andreaus

Department of Structural and Geotechnical Engineering, Sapienza University of Rome, Via Eudossiana 18, Rome 00148, Italy

ARTICLE INFO

Keywords:
Linear isolation (LI)
Harmonic base excitation
Unilateral deformable and dissipative constraints
Vibro-impact isolation system (V-IIS)
Optimal design
Steady-state response
Transient response
Static displacement
Transmissibility
Displacement response factor

ABSTRACT

Seismically isolated structures can be subjected to large horizontal displacements relative to the ground, especially in Near-Fault earthquakes, which are characterized by one or more intense pulses of velocity and displacement of long period. One strategy to mitigate the problem of large displacements, which occurs in linearly isolated structures, is the use of deformable and dissipative devices (bumpers). The impact between the structure and the bumpers, if the bumpers are appropriately designed, can produce beneficial effects on the dynamic response of the system, both on displacements and accelerations. In this paper the response obtained from a numerical model of isolated single-degree-of-freedom (SDOF) systems constrained by two bumpers, arranged symmetrically on both sides of the mass of the system with an initial gap, subjected to base harmonic excitation, is studied. This model is called Vibro-Impact Isolation System (V-IIS). The objective of this work is to define a methodology for choosing the design parameter defining the V-IIS (mechanical characteristics of the bumpers, gap and isolation frequency of the system) by observing both steady-state and transient responses of both the system and the bumpers. The study of the transient response is compared with that obtained in the steady-state to assess how representative the latter is of the V-IIS transient response. From the definition of the methodology for choosing the parameters of the V-IIS, through optimal design, the only design parameters are the gap and the isolation frequency of the system. Therefore, an appropriate choice of the gap makes it possible to bring frequency-selective viscous damping in V-IISs, introducing two advantages over linear systems: the reduction of the peak intensity of the responses in the resonance range (both displacement and acceleration) and the reduction of the static displacement of the system, but keeping the dynamic response with which the system is designed unchanged.

1. Introduction

One of the most widely used strategies for passively controlling the dynamic response of sensitive structures and equipment is base isolation. This strategy consists of interposing a highly deformable element horizontally between the base floor and the structure (or equipment), so as to significantly increase the period of the system and reduce the transmitted acceleration.

The problems of traditional (i.e. linear) isolated systems are due to their low stiffness, which induces large displacements of the isolated floor, with respect to both static actions and seismic events characterized by several long-period displacement and velocity pulses (Near-Fault earthquakes) [1,2]. These large displacements can cause two different problems: exceeding the limit deformation of the isolators, and thus inducing permanent deformation or rupture of the isolators; or impact of the isolated structure or equipment with adjacent elements, if the space between them, the gap, is not sufficient to accommodate the large displacements generated [3,4]. In the latter case, inadequate gap sizing may be due to practical limitations, for example, for seismic isolation retrofitting of existing buildings in metropolitan areas, where adequate space is not always available. Pounding has been shown to generate increases in both accelerations and interstorey drifts in isolated structures that impact surrounding space walls [4,5]. These increases in dynamic response can cause severe damage to structural and nonstructural elements [6,7], such as sensitive equipment located within the isolated buildings [8,9]. The problems caused by large displacements can also be due to the presence of vibrating machines, which during their on–off phases or not working under design conditions, can attain frequency values close to those of resonance, transmitting strong accelerations and displacements to the structures that contain them, creating discomfort

* Corresponding author.
E-mail addresses: giuseppe.perna@uniroma1.it (G. Perna), maurizio.deangelis@uniroma1.it (M. De Angelis), ugo.andreaus@uniroma1.it (U. Andreaus).

https://doi.org/10.1016/j.istruc.2023.105270
Received 5 May 2023; Received in revised form 18 September 2023; Accepted 18 September 2023
Available online 10 October 2023

[10,11].

Some studies, focusing on reducing the large static displacements of linear isolation systems, propose nonlinear isolation systems with high static stiffness and low dynamic stiffness [12,13]. These systems take advantage of negative stiffness mechanisms (NSMs) arranged in parallel with classical isolation systems. Subsequent developments of these systems led to the definition of nonlinear isolators as quasi-zero stiffness (QZS) systems [10,11].

In contrast, semi-active control systems, through the use of sensors, processors and actuators, allow the mechanical parameters (such as stiffness [14]) of control devices to be adjusted in real time so limiting problems due to large displacements.

Another effective strategy to reduce and control the negative effects due to large displacements of the isolation floor is the interposition of deformable and dissipative devices, called bumpers [15,16]. Polycarpou and Komodromos [17] studied, through numerical simulations, the effectiveness of using rubber bumpers, to be applied at locations where impacts are likely to occur, to act as shock-absorbers.

De Angelis and Andreaus conducted several experimental investigations on the influence of bumpers on the dynamic response of single-degree-of-freedom (SDOF) systems subjected to harmonic base excitation [18–26]. From these studies, it was observed that the parameters governing the impact between the system and the bumper can be summarized into three: gap (distance between mass and bumper), stiffness and damping of the bumpers. In addition, the authors, based on the experimental investigations, defined a numerical model, through which numerical analyses [18,21,24] were carried out, which allowed the identification of optimality relationships between stiffness and damping coefficient of the bumper and ratio damping of the system, reducing the design parameters from three to two [26]. These works [19–23,25] will be discussed in more detail in Section 4.

The present work analyzes the response obtained from a numerical model of isolated SDOF system constrained by two bumpers, arranged symmetrically on both sides of the mass of the system with an initial gap, subjected to basic harmonic excitation. This model, thus defined, takes the name of Vibro-Impact Isolation System (V-IIS).The design of the bumpers is carried out following the optimality relationship introduced in [26] and an optimal curve presented in this paper. Therefore, the objective of this work is to define a methodology for choosing the design parameter defining V-IIS (gap and system isolation frequency) by observing both steady-state and transient responses of both the system and the bumpers. The study of the transient response is then compared with that obtained previously at steady-state to value how representative the latter can be of the response of V-IIS to transient as well. Although this methodology is obtained through the study of SDOF oscillator subjected to a harmonic base excitation, it also shows applicability in the case of seismic motion in the ground. This is because for a seismic excitation, although it is a multi-frequency action, it can be assumed that its action on a structure can be characterized by a quasi-resonant state at the effective fundamental frequency of the structure. These proposed nonlinear isolation systems, in reducing large displacements by introducing a limit switch to the isolated system, allow the dynamic amplification in the resonance range and the static displacement to be reduced.

Section 2 introduces the linear oscillator focusing on the influence of the damping and isolation frequency at which the system is designed; Section 3 introduces the model with the equations of motion; Section 4 reports the authors' contributions about Vibro-Impact Systems both on the study of nonlinear dynamics and possible response scenarios and, subsequently, on the control of dynamic response; Section 5 talks about the design criteria of the parameters of V-IISs, introduces the optimal design of the bumpers and a study on the influence of the gap and the isolation frequency on the response; Section 6 reports the steady-state responses, obtained in terms of Pseudo-Resonance Curves (PRCs), in which the sweeps were carried out by applying the continuation technique, and the transient responses, obtained through time histories and force–displacement cycles, for four different initial gaps and without impact condition; finally, Section 7 concludes by reporting final considerations on the results obtained. All reported results are also represented in dimensionless terms so that they can be generalized.

2. Linear isolation systems

A simple single-degree-of-freedom oscillator, such as a mass-spring-damper system, is introduced to study linear isolated systems and to define what the criticality of these systems depends on.

The graph in Fig. 1 shows the transmissibility of acceleration $TR_a(\xi, \beta)$ [27] as a function of parameter β, for different values of parameter ξ: $TR_a(\xi, \beta)$ represents the maximum absolute acceleration a_0 transmitted to a mass normalized with respect to the peak ground acceleration A_G; β is defined as the ratio of the frequency Ω of the harmonic excitation to the frequency ω of the system; ξ is the damping ratio defined as the ratio of the damping coefficient c to the critical damping coefficient $c_{cr} = 2m\omega$.

The analytical formula of the transmissibility of acceleration is as follows:

$$TR_a(\beta, \xi) = \frac{a_0}{A_G} = \sqrt{\frac{1 + (2\beta\xi)^2}{\left(1 - \beta^2\right)^2 + (2\beta\xi)^2}} \tag{1}$$

From the study of the curve, two ranges can be identified. These are separated by the value $\beta = \sqrt{2}$, which together with $\beta = 0$ identify the two fixed points where transmissibility takes a unity value, i.e., transmitted acceleration a_0 is equal to ground acceleration A_G:

- $0 \le \beta \le \sqrt{2}$ non-isolation range, where transmissibility is greater than or at most equal to 1;
- $\beta > \sqrt{2}$ range of isolation, where transmissibility is less than 1.

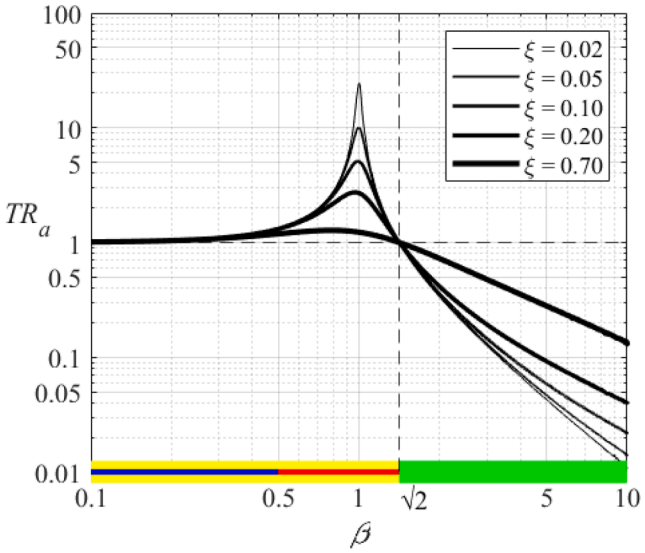

Fig. 1. Transmissibility TR_a curves, representing the ratio of the amplitude of the absolute acceleration of the single-degree-of-freedom oscillator a_0 to the amplitude of the absolute acceleration of the ground motion A_G, as a function of the ratio β of the harmonic forcing frequency to the oscillator frequency and for five different values of the system damping ratio ξ (smaller thicknesses represent smaller damping ratios) are shown. $0 < \beta \le \sqrt{2}$ represent the non-isolation range, highlighted in yellow; $\beta > \sqrt{2}$ represent the isolation range, highlighted in green. The non-isolation range is in turn divided into a quasi-static response sub-range (for small β values), highlighted in blue, and a resonance sub-range (for β values around 1), highlighted in red. (For interpretation of the references to color in this figure legend, the reader is referred to the web version of this article.)

As shown in Fig. 1, the first range can be further divided into two sub-ranges that are not well defined:

- β small, quasi-static response sub-range, where the amplitude of the transmitted acceleration is essentially equal to the peak ground acceleration;
- β approximately larger than 0.5 but smaller than $\sqrt{2}$, resonance sub-ranges, within which the mass response is amplified, attaining a maximum in $\beta_R = \sqrt{1-2\xi^2}$.

It is also observed that ξ acts over the entire range of β, reporting different effects in the two ranges of β: in the range $0 \le \beta \le \sqrt{2}$ it acts positively by reducing the response as damping increases; in $\beta > \sqrt{2}$, it acts negatively by increasing the response, thus reducing the effectiveness that is achieved in isolation, again as damping increases.

While the Transmissibility curves quantify the acceleration transmitted to the mass, the displacement response factor curves $R_d(\xi,\beta)$ (Fig. 2) show the maximum displacement u_0 of the system subjected to harmonic forcing compared to the displacement u_{st} that is obtained with a static force of intensity equal to the amplitude of the harmonic forcing.

The analytical formula of the displacement response factor is as follows:

$$R_d(\beta,\xi) = \frac{u_0}{u_{st}} = \frac{1}{\sqrt{\left(1-\beta^2\right)^2+(2\beta\xi)^2}} \tag{2}$$

The same β ranges identified in Fig. 1 are also given for the response quantity R_d:

- If $\beta \ll 1$, sub-range of quasi-static response, $R_d \simeq 1$, then the dynamic displacement is approximately equal the static displacement for any value of ξ;
- when β is contained in the resonance sub-range, R_d is very sensitive to the change in the damping ratio of the system, taking increasing values as ξ decreases;
- if $\beta \gg 1$, isolation range, R_d tends to zero for any value of ξ.

Therefore, the damping ratio acts positively over the whole range of β. However, while in the resonance sub-range the response is very sensitive to the variation of ξ, the response decreases as the damping increases, in the quasi-static response sub-range and in the isolation range, the influence of ξ on the response is negligible.

From the study of TR_a and R_d, both problems related to the non-isolation range and to the isolation range emerge. For values of β characteristic of the resonance sub-range, the system exhibits high amplifications of the maximum responses in terms of both displacement and acceleration. To overcome this problem, action is taken by increasing either the damping ratio ξ, reducing the maximum response values, or the isolation β, β_I, ratio of system operating frequency moving away from the resonance range and toward lower response values.

In the isolation range, on the contrary, as ξ increases, the beneficial effect of isolation is reduced.

The static displacement, on the other hand, as normalized in Fig. 2, depends neither on the β of isolation, β_I, nor on ξ; therefore, it is free from problems. In fact, the quantity R_d, characterizing the maximum displacement response of the system, allows the static displacement to be read in the quasi-static response sub-range, with $\beta \ll 1$, and is equal to the unit value for each ξ.

The curve in Fig. 3 is now introduced in which the dimensionless static displacement q^*_{st}, defined as the ratio of the static displacement $u_{st} = A_G/\omega^2$, equal to the peak ground acceleration A_G divided by the square of the frequency ω of the system, and the peak ground displacement $D_G = A_G/\Omega^2$, equal to the peak ground acceleration A_G

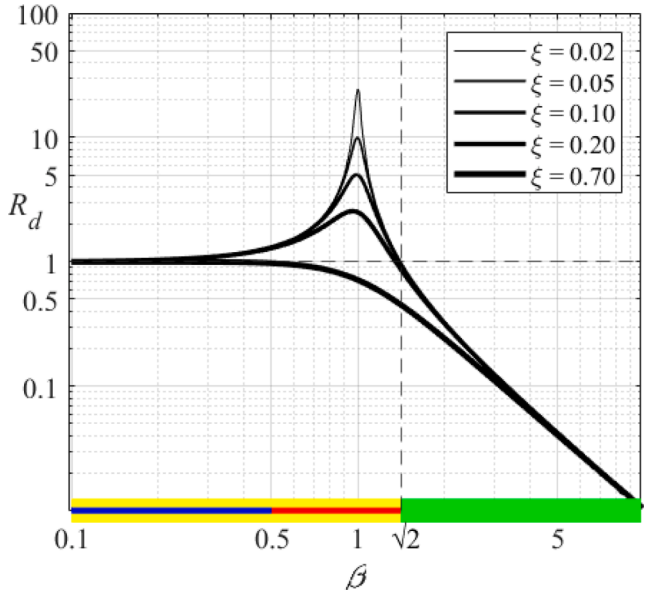

Fig. 2. Displacement response factor R_d, representing the ratio of the amplitude of the relative displacement u_0 to the static displacement due to a force equal to $A_G \bullet M$, of the single-degree-of-freedom oscillator, as a function of the ratio β of the harmonic forcing frequency to the oscillator frequency and for five different values of the system damping ratio ξ (smaller thicknesses represent smaller damping ratios) are shown. $0 < \beta \le \sqrt{2}$ represent the non-isolation range, highlighted in yellow; $\beta > \sqrt{2}$ represent the isolation range, highlighted in green. The non-isolation range is in turn divided into a quasi-static response sub-range (for small β values), highlighted in blue, and a resonance sub-range (for β values around 1), highlighted in red. (For interpretation of the references to color in this figure legend, the reader is referred to the web version of this article.)

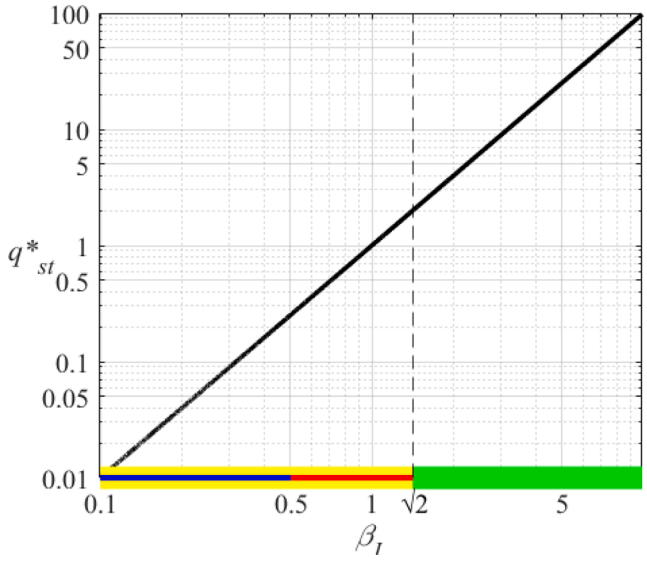

Fig. 3. Static dimensionless displacement q^*_{st}, representing the ratio of the static displacement of the single-degree-of-freedom oscillator u_{st}, due to a force equal to $A_G \bullet M$, to the amplitude of the displacement of the ground motion D_G, as a function of the isolation frequency ratio β_I of the oscillator is shown. $0 < \beta \le \sqrt{2}$ represent the non-isolation range, highlighted in yellow; $\beta > \sqrt{2}$ represent the isolation range, highlighted in green. The non-isolation range is in turn divided into a quasi-static response sub-range (for small β values), highlighted in blue, and a resonance sub-range (for β values around 1), highlighted in red. (For interpretation of the references to color in this figure legend, the reader is referred to the web version of this article.)

divided by the square of the frequency Ω of the excitation, as a function of the parameter β_I, is reported. This β_I represents the isolation frequency ratio that characterizes the system, so the range of interest is that of isolation relative therefore to values of $\beta > \sqrt{2}$.

The function describing q^*_{st} is:

$$q^*_{st} = \frac{u_{st}}{D_G} = \beta^2 \tag{3}$$

It is evident from Fig. 3 that the design of systems with high β_I leads to high values of the static displacement.

As known, the response of linear systems depends on two parameters: the frequency ratio β and the damping ratio ξ. The first parameter β allows us to define response ranges (quasi-static, resonance, and isolation); the second parameter ξ influences the resonance and isolation ranges in a more or less beneficial way. An appropriate choice of parameter β, toward high values, allows reducing the response; on the contrary, high values of parameter ξ reduce the response in the resonance range and increase it in the isolation range.

A linear system that exhibits low response values, therefore, turns out to be designed with high values of β, in the isolation range, and with modest values of ξ. Systems designed in this way, linear isolated systems, present problems both with respect to static displacement, since high values of β result in high values of static displacement, and during the application of the excitation, in the transient before the excitation attains the steady-state. This is because, during the application of the excitation, the system, in reaching steady-state, spans all values of β between 0 and the value of β isolation, β_I, with which the isolated system is designed. The system then, in the transient, also assumes values of β close to resonance, albeit for a limited time range, which result in high values of response as it presents small values of ξ.

One possible solution to the problems that arise in linear isolated systems may be to define a new nonlinear isolated system. The nonlinear behavior, introduced by β-selective damping, should produce two beneficial effects: limit the dynamic amplification in the non-isolation range; increase the static stiffness without changing the behavior of the system in the isolation range.

3. Model and equations of motion

The model adopted for numerical analysis is illustrated in Fig. 4. The figure represents a Vibro-Impact single-degree-of-freedom (SDOF) system consisting of a mass M, a damper D, and two deformable and dissipative bumpers, arranged symmetrically on both sides of the mass with an initial gap G_{0j} ($j = R$ right side, $j = L$ left side) and referred to as right bumper B_R and left bumper B_L, respectively. The damper and

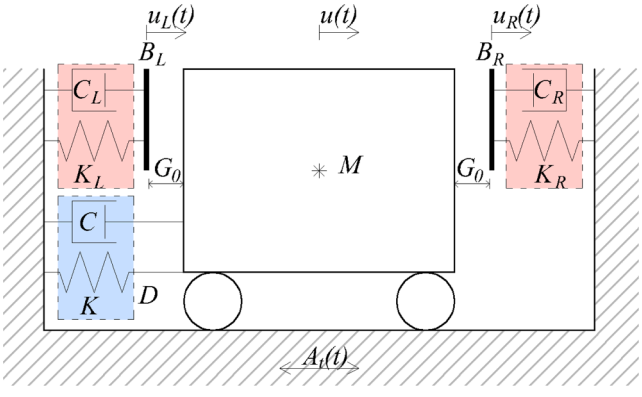

Fig. 4. Model of the system: the cyan box contains the mechanical elements that characterize the damper, and the red boxes contain the mechanical elements that characterize the bumpers. (For interpretation of the references to color in this figure legend, the reader is referred to the web version of this article.)

bumpers are modeled by a linear elastic element, with stiffness K and K_j ($j = R, L$), respectively, and a linear viscous damper, with damping coefficient C and C_j ($j = R, L$), respectively, arranged in parallel. The system is subjected to a harmonic base acceleration $A_t(t) = A_G \sin(\Omega t)$, where A_G is the amplitude and Ω the circular frequency of this excitation. Finally, in Fig. 4 $u(t)$ refers to the relative displacement of the mass with respect to the ground, and $u_j(t)$ ($j = R, L$) refers to the bumper deformation.

The equation of the motion is written in dimensionless form to make them as general as possible. The components of the equation are normalized with respect to $F^* = M\omega^2 u^*$, which represents the maximum force in the SDOF system in free flight (without impact, FF): the quantity $u^* = u_{st} \bullet R_{d,max}$ represents the maximum relative displacement in FF, where $u_{st} = A_G/\omega^2$ is the static displacement and $R_{d,max} = 1/(2\xi\sqrt{1-\xi^2})$ is the maximum value of the displacement response factor $R_d(\xi, \beta)$; while $\omega = \sqrt{K/M}$ denotes the frequency of the system. The frequency ratio $\beta = \Omega/\omega$ and the damping ratio $\xi = C/2M\omega$ are introduced, and the dimensionless time $\tau = \omega t$ is defined. In the dimensionless equations, the quantities $q = u/u^*$ and $q_j = u_j/u^*$ ($j = R, L$) are the dimensionless displacement of the mass and the dimensionless deformation of the bumpers, respectively. Similarly, the dimensionless gap is $\delta_{0j} = G_{0j}/u^*$ ($j = R, L$) and can take values in the range $0 \le \delta_{0j} \le 1$. The force $f(\tau) = 2\xi q'(\tau) + q(\tau)$ is the dimensionless force of the damper, while $f_j(\tau) = 2\xi\gamma_j q'_j(\tau) + \lambda_j q_j(\tau)$ ($j = R, L$) – where $\gamma_j = C_j/C$ and $\lambda_j = K_j/K$ are the dimensionless damping and dimensionless stiffness of the bumpers – are dimensionless contact forces. Finally $a_t(\tau) = a_G sin\beta\tau$ is the dimensionless harmonic excitation, where $a_G = 2\xi\sqrt{1-\xi^2}$ is the dimensionless amplification, and $\alpha(\tau) = q''(\tau) + a_t(\tau)$ is the total or absolute acceleration of the mass.

Therefore, the dimensionless equations of motion of the model can be written in the following form:

$$\begin{cases} q''(\tau) + f(\tau) + f_j(\tau) \bullet \psi_1[\delta_j(\tau)] \bullet \psi_2[f_j(\tau)] = -a_G sin\beta\tau \\ f_i(\tau) = 0 \end{cases} \tag{4}$$

where it is assumed that, if the mass is in contact with the left bumper, $j = L$ and $i = R$, or, if the mass is in contact with the right bumper, $j = R$ and $i = L$. In the equations the Heaviside functions ψ_1 and ψ_2 are defined as follows:

$$\text{contact } \psi_1[\delta_j(\tau)] = \begin{cases} 0, \delta_j(\tau) > 0 \\ 1, \delta_j(\tau) = 0 \end{cases} \quad (j = R, L) \tag{5}$$

$$\text{separation } \psi_2[f_j(\tau)] = \begin{cases} 0, f_R(\tau) \le 0 \text{ or } f_L(\tau) \ge 0 \\ 1, f_R(\tau) > 0 \text{ or } f_L(\tau) < 0 \end{cases} \tag{6}$$

where $\delta_j(\tau)$ ($j = R, L$) represents the gap function in terms of dimensionless time τ and, if $j = R$, is equal to $\delta_R(\tau) = \delta_{0R} + q_R(\tau) - q(\tau)$, and, if $j = L$, is equal to $\delta_L(\tau) = \delta_{0L} - q_L(\tau) + q(\tau)$. In all introduced equations the superscript (′) indicates the differentiation with respect to dimensionless time τ.

Since the bumpers are equal and symmetrically arranged on both sides of the mass $\gamma_R = \gamma_L = \gamma$, $\lambda_R = \lambda_L = \lambda$ and $\delta_{0R} = \delta_{0L} = \delta_0$.

4. Nonlinear vibro-impact isolation systems: linear isolated systems with vibro-impact systems

Linear isolation systems show problems related to large displacements, since they have high isolation frequency ratios β_I, and to the presence of excessive response values when working in the resonance zone, due to modest damping ratios ξ. Therefore, introducing appropriately designed end-stop devices (bumpers) to linear isolation systems, in addition to making the system strongly nonlinear, allows these problems to be mitigated.

The authors have extensively studied, both numerically

[18,21,23–26] and experimentally [19–23,25], the dynamic response of Vibro-Impact isolated systems, via single-degree-of-freedom (SDOF), base-isolated systems constrained on both side with bumpers.

Initial numerical studies performed in [18] showed the influence of bumpers mechanical characteristics on the dynamic response of the system defining the various scenarios. Fore and back sweeps in acceleration and relative displacement excursion were performed, applying the continuation technique. These analyses revealed the presence of multiple resonance peaks, hysteresis ranges, and jumps between different solutions. Based on this numerical study, subsequent experimental work presented in [19,20] was directed. Specifically, the first paper [19] was used to verify the operation of the experimental equipment and test the feasibility of the designed experiments using only one type of bumper, one gap width, and four peak values of table acceleration. The second work [20] was devoted to individually characterize the mechanical behavior of the damper and bumpers prior to shake-table tests also in relation to strain rate and to verify potential differences in the dynamic response of the system with respect to different bumpers, gaps, and peak table accelerations; for this purpose, two types of bumpers, two gap values for each type of bumper, and at most four peak table acceleration values were used in the case of one bumper and one gap. In [21] the results of an additional experimental work were presented in which the experimental setup of the previous experiments was improved. The results obtained from these experimental tests [19–21] showed excellent agreement with the numerical results obtained in [18]. In [23], the focus is on identifying and characterizing the possible scenarios that can occur in the experimental response of the single-degree-of-freedom (SDOF) Vibro-Impact Isolation System (V-IIS) by varying the peak value of the table acceleration, the initial gap between mass and bumper, and the bumper stiffness. Four scenarios were identified: scenario corresponding to the free-flight condition FF; scenario corresponding to the grazing condition; scenario characterized by the presence of only the primary resonance with right hysteresis; and scenario that compared to the previous one also has a the secondary resonance. These scenarios were also reproduced numerically using a Simplified Nonlinear Model (SNM). In [24] further numerical analyses were conducted by studying small and null gaps. These analyses allowed additional scenarios to be added to the scenarios obtained in [23]. Therefore, this study motivated the experimental work presented in [25] that investigated the influence of the gap parameter on the dynamic response of V-IIS, confirming the results obtained in [24] and extending the parametric investigation by considering positive, zero and negative gaps.

The definition of the SNM allowed characterizing the impact phenomenon by defining three parameters: the dimensionless gap δ_0, the dimensionless stiffness λ and the dimensionless damping γ.

Based on the response scenarios identified in some of the works [18–21,23–25], successive experimental and numerical studies have dealt with vibration control [22,26], particularly on the appropriate choice of the values of the three parameters gap, stiffness and damping of the bumpers, which allow both large displacements and excessive accelerations to be mitigated. The paper [22] reports the results of an experimental campaign on a shaking table of a SDOF system symmetrically constrained by two bumpers. This study brought out how a correct choice of bumpers and seismic gap allows a better control of the response in both displacement and acceleration. This result directed the studies presented in [26], which are an extension of [22]. The objective of this work [26] is to investigate, via parametric numerical analysis, the possibility of using impact to control the dynamic response of isolated systems. This objective was partially achieved through the definition of an optimality relationship that allows selection of bumper stiffness as a function of bumper damping and system damping ratio. This optimality relationship is presented in Subsection 5.1.

In this work, an additional constraint is added to the design of bumpers that bonds the stiffness of bumpers with the gap through an optimal curve. Therefore, an optimal design methodology has been defined that links the three parameters defining the impact phenomenon (δ_0, λ, γ), by means of an optimality relationship [26] and an optimal curve, thus reducing the design of V-IISs to the selection of the gap parameter δ_0 and the isolation frequency of system β_I. In this way a new vibration control methodology is defined. It involves coupling linear isolated systems with bilateral constraints composed of deformable and dissipative devices, called Vibro-Impact Isolation Systems (V-IISs). The nonlinear behavior of the V-IISs, achieved by the presence of additional β-selective viscous damping that is controlled by the appropriate choice of the parameters λ, γ and δ_0, allows two benefits to be introduced to linear systems: reducing the peak intensity of the responses in the resonance range and reducing the static displacement of the system.

This result makes it possible to exploit both the benefits of isolated systems, in the range of isolation frequencies, and the benefits due to viscous energy dissipation through the use of bumpers, in the non-isolation range. Therefore, the bumpers can have a selective influence in the frequency range limited to the non-isolation range.

5. Design criteria of the parameters of V-IISs

When designing the V-IISs, both the parameters that characterize the phenomenon of the impact of the mass with the bumpers and the isolation frequency of the system must be defined. The parameters related to the impact are the dimensionless gap δ_0, the dimensionless stiffness of the bumpers λ and the dimensionless damping of the bumpers γ. The design of these parameters is done through an optimality relationship, reported in [26], and an optimal design curve, presented in this work, which allow to design the bumpers in an optimal way through the choice of the δ_0 parameter alone. Instead, as regards the isolation frequency of the V-IISs, the fundamental design parameter is the isolation frequency ratio β_I. Therefore, the design of the V-IISs is delegated to the choice of the parameters δ_0 and β_I only. A right choice of these parameters allows to reduce the amplitude of the acceleration in resonance and the static displacement of the system.

The definition of the optimality curve and the study of the influence that the parameters δ_0 and β_I have on the response of the system, were done through the study of Pseudo-Resonance Curves (PRCs) of the normalized excursions of the absolute acceleration $\eta_a = \Delta\alpha/\Delta\alpha_0$ and of the relative displacement $\eta_d = \Delta d/\Delta d_0$, where the excursions $\Delta\alpha$ and Δd are calculated as the difference between the maximum and minimum values recorded in the steady state of each frequency sub-interval of the absolute acceleration and of the relative displacement, respectively; while, $\Delta\alpha_0$ and Δd_0 are the maximum excursions of the absolute acceleration and of the relative displacement in free-flight conditions FF, respectively.

Subsection 5.1 will therefore report the optimal design of the bumpers, while Subsection 5.2 will report a study on the influence of the two free design parameters, δ_0 and β_I, providing indications on the influence of two parameters on the system response by identifying outlier values.

5.1. Optimal design of the bumpers

In order to optimize the control of the dynamic response of the system, an optimal design criterion for selecting the physical parameters governing the impact (gap δ_0, stiffness λ and damping γ of the bumpers) is adopted. This is based on an optimality relationship, introduced in [26], that bonds the damping ratio ξ of the system with the parameters λ and γ of the bumpers, and an optimal curve, introduced in this paper, in which the stiffness λ of the bumper is a function of the gap δ_0.

The optimality relationship is defined as follows:

$$\frac{\gamma}{\lambda} = \frac{1}{2\xi} \tag{7}$$

This relationship was sought through a parametric numerical analysis in which, for each δ_0 investigated and for fixed values of ξ and γ, the value of λ was found such that the peak acceleration of the mass in

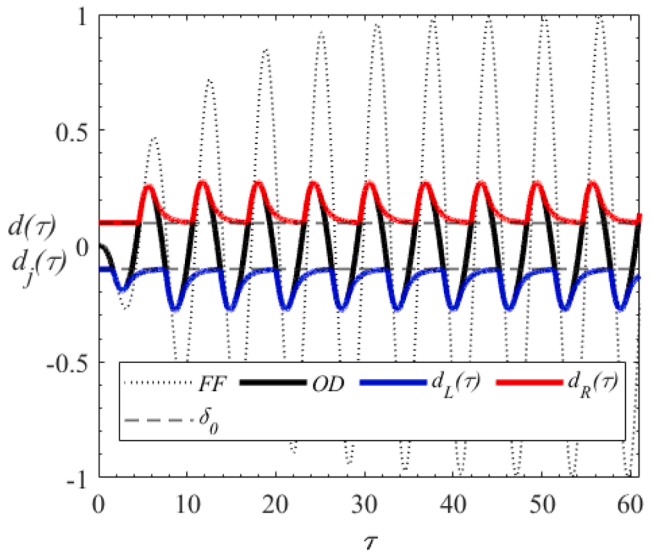

Fig. 5. Time history of displacement: in black (impact with optimal bumper design, *OD*) and dashed black (without impact, *FF*) the trend of mass position $d(\tau) = q(\tau)$; in blue ($j = R$) and red ($j = L$) the trend of bumper position $d_R(\tau) = q_R(\tau) + \delta_0$ and $d_L(\tau) = q_L(\tau) - \delta_0$. The system has $\xi = 0.10$ and the *OD* parameters are $\delta_0 = 0.10$, $\lambda = 0.78$ and $\gamma = 3.90$ (obtained by the optimality relation, Eq. (7)). (For interpretation of the references to color in this figure legend, the reader is referred to the web version of this article.)

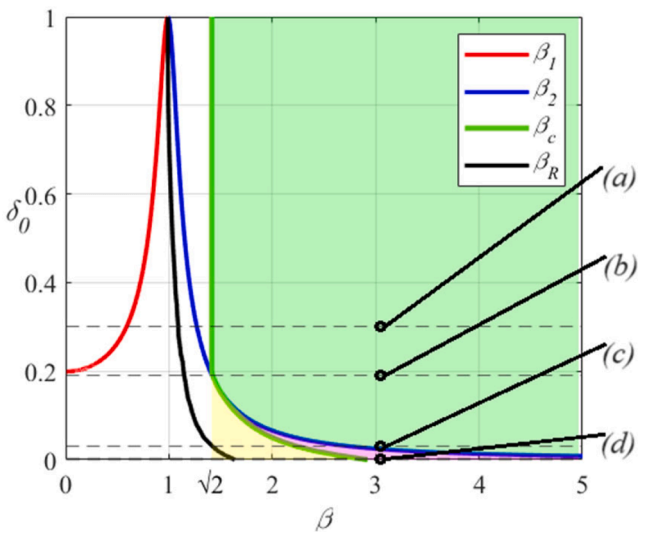

Fig. 7. Trends of the characteristic β values with the dimensionless gap δ_0: red line β_1 represents a limit curve that, for $\beta < \beta_1$, returns the no-impact scenarios; blue line β_2 represents the limit curve that, for $\beta > \beta_2$, returns the no-impact scenarios; the black line β_R represents the β values of resonance; green line β_c represents the β values of isolation beginning. The colored areas represent different situations which can occurs when $\beta > \sqrt{2}$: green area represents no-impact scenarios; magenta area represents scenarios where the amplitude of mass acceleration is lower than the amplitude of ground acceleration, but is still greater than the acceleration under free-flight conditions; yellow area represents scenarios where the amplitude of the mass acceleration is greater than the acceleration amplitude of the ground and of the mass in free-flight condition. The dotted lines show the δ_0 investigated in Fig. 8: *(a)* $\delta_0 = 0.3$, *(b)* $\delta_0 = 0.19$, *(c)* $\delta_0 = 0.03$, *(d)* $\delta_0 = 0$. (For interpretation of the references to color in this figure legend, the reader is referred to the web version of this article.)

resonance was minimized. This is possible because the bumpers are fully utilized: as show in Fig. 5, the bumpers have sufficient time to recover their deformation before the next impact, dissipating all the accumulated energy, and they do not remain inactive because the next impact occurs practically immediately after recovery; therefore, the analytical definition Eq. (7) was obtained by imposing the dimensionless bumper relaxation time $\tau_r = 1$, with $\tau_r = 2\xi\gamma/\lambda$.

The optimality relationship (Eq. (7)) is independent of the gap and through it, it is possible to reduce the number of impact parameters from three (δ_0, λ, γ) to two, since choosing λ gives the value of the corresponding γ.

With the introduction of the optimal curve (Fig. 6a) an additional constraint is introduced, reducing the bumper design to the choice of only one parameter, the dimensionless gap δ_0. The optimal curve, shown in Fig. 6a, was obtained through a parametric analysis by which for each δ_0 and for a fixed value of ξ, the optimal value λ_{opt}, and then through the optimality relationship (Eq. (7)) also of γ_{opt}, is found such that the maximum acceleration of the system is minimized (Fig. 6b, obtained for a value of δ_0 equal to 0.10).

Therefore an optimal procedure was applied to minimize the maximum of the objective function η_a, which represents the normalized excursion of the absolute acceleration of the mass. The optimization problem is to find the parameter λ bounded within a predetermined searching range [0.01 10], for any values of δ_0 within the range [0 1], for γ dependent on λ as it is subject to the optimality relationship Eq. (7) and for a fixed value of $\xi = 0.10$. therefore, this procedure can be expressed mathematically in the form:

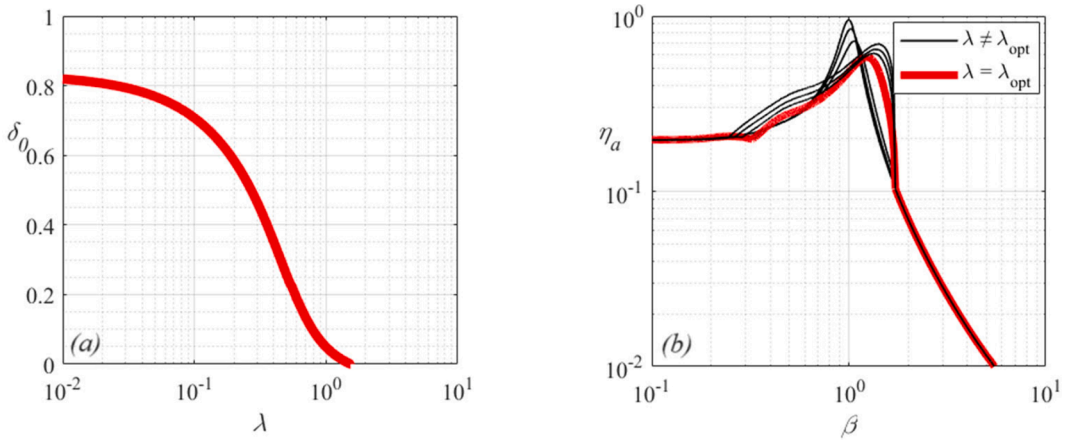

Fig. 6. (*a*) Optimal curve that associates each gap δ_0 with an optimal value of the stiffness of the bumper λ_{opt}; (*b*) Pseudo-Resonance Curves (PRCs) in acceleration η_a for $\delta_0 = 0.10$ and for different values of the stiffness of the bumper λ: in red PRC obtained with λ_{opt}, while in black PRCs obtained with values of λ other than the optimal one. (For interpretation of the references to color in this figure legend, the reader is referred to the web version of this article.)

$$0 \leq \delta_0 \leq 1 \text{ find}_{\lambda} \, min \, max \, \{\eta_a[\lambda \, | \delta_0 \, \gamma \, \xi]\} \tag{8}$$

$$\text{subjected to} \begin{cases} 0.01 \leq \lambda \leq 10 \\ \xi = 0.1 \\ \gamma = \dfrac{\lambda}{2\xi} \end{cases} \tag{9}$$

Looking at the red curve in Fig. 6a, it is evident that controlling the response of the Vibro-Impact system with a gap $\delta_0 > 0.82$, is ineffective. This is because, for these values of δ_0, the optimal stiffness λ is so small that the presence of the bumpers is insignificant.

This optimal design allows the bumper design parameters to be reduced from three to one, the dimensionless gap δ_0 alone. However, the overall response of V-IIS also depends on the choice of system isolation frequency β_I, so the influence of these two parameters (δ_0 and β_I) on the response will be discussed in the following subsection.

5.2. Influence of parameters δ_0 and β_I on the response

Fig. 8 shows the trend of some characteristic values of β in terms of dimensionless gap δ_0, in the optimal design (minimum peak of excursion of mass acceleration) and with a damping ratio $\xi = 0.10$.

Specifically, the red and blue lines represent the values, denoted β_1 and β_2, respectively, which identify the boundaries of the frequency range ($\beta_1 < \beta < \beta_2$) where, for the considered value of δ_0, impact definitely occur, based on purely geometric considerations. The black and green lines, refer to the β_R and β_c values, which indicate, for the considered value of δ_0, the resonance frequency and the frequency at which the isolation range begins, respectively. While the values of β_1 and β_2 depend only on ξ and δ_0, the values β_R and β_c also depend on λ and γ.

It can be observed that β_R (black curve), starting from $\beta_R \simeq 0.99$ for $\delta_0 = 1$ (free-fight condition), increases as δ_0 decreases, reaching its maximum value ($\beta_R \simeq 1.70$) for $\delta_0 = 0$. This is also evident from Fig. 8a-d, in which, for selected values of δ_0 (0.3 in Fig. 8a, $\delta_{0c} \simeq 0.19$ in Fig. 8b, 0.03 in Fig. 8c, 0 in Fig. 8d), the PRCs of η_a (left column) and η_d (right column) are shown, considering both the free-flight condition FF (black curve) and the condition corresponding to the minimum peak acceleration value (red curve, optimal condition). In these figures, the above-mentioned frequency values are represented with colored symbols (β_1 cyan diamond, β_2 cyan circle, β_R black circle, β_c green triangle) and the yellow boxes represent the values of η_a and η_d for $\beta = 0$.

As for β_1 (red curve in Fig. 7) and β_2 (blue curve in Fig. 7), these coincide ($\beta_1 = \beta_2 \simeq 0.99$) for $\delta_0 = 1$ (FF) and increasingly diverge as δ_0 decreases, with $\beta_1 < 0.99$ and $\beta_2 > 0.99$. For $\delta_0 = \delta_0^* \simeq 0.199$, impact occurs immediately ($\beta_1 = 0$). For $0 \leq \delta_0 < \delta_0^*$, impact still occurs from $\beta_1 = 0$, but, compared to the case $\delta_0 = \delta_0^*$ the equation $R(\xi, \beta) = \delta_0$ (where $R(\xi, \beta)$ is the displacement response factor $R_d(\xi, \beta)$ normalized with respect to its maximum value $R_{d,max}(\xi)$) admits only one solution, that is β_2 (blue curve). Finally, when the bumpers are initially in contact with the mass ($\delta_0 = 0$), the equation $R(\xi, \beta) = \delta_0$ admits no solution and thus impact occurs for any value of β. This is also evident from Fig. 8a-d. In particular, the symbols representing β_1 and β_2 (cyan diamond and cyan circle, respectively) are both visible for $\delta_0 = 0.3$ (first row, Fig. 8a), while for $\delta_0 = \delta_c \simeq 0.1915$ (second row, Fig. 8b) and for $\delta_0 = 0.03$ (third row, Fig. 8c) only β_2 (cyan circle) appears. For $\delta_0 = 0$ (fourth row, Fig. 8d) there is no symbol.

These values of β (β_1, β_2, β_c) and δ_0 (δ_0^*, δ_{0c}) define outliers, in that different responses occur if the parameters β_I and δ_0 take values greater or less than these. Therefore, the different response ranges defined by these outliers will be discussed below. In fact, referring to the frequency value (isolation threshold) beyond which, where the impact occurs, the amplitude of the mass acceleration becomes lower than the amplitude of the ground acceleration, denoted as β_c and represented with a green line in Fig. 7 (and with a green triangle in the PRCs shown in Fig. 8a-d), two ranges can be identified, namely $\delta_{0c} < \delta_0 \leq 1$ and $0 < \delta_0 < \delta_{0c}$.

For $\delta_{0c} < \delta_0 \leq 1$ (see also Fig. 8a, corresponding to $\delta_0 = 0.3$), $\beta_c = \sqrt{2}$, which means that, in the presence of obstacles, the frequency range where $\eta_a < \eta_a|_{\beta=0}$ (highlighted in green) is the same as in the linear case (FF). Consequently:

- for $0 \leqslant \beta < \beta_1$ the impact does not occur and thus the system behaves as a linear system; moreover, $\eta_a > \eta_a|_{\beta=0}$;
- for $\beta_1 \leqslant \beta < \beta_2$ the impact definitely occurs and it is still $\eta_a > \eta_a|_{\beta=0}$;
- for $\beta_2 < \beta < \beta_c$ the impact does not occur and therefore the system behaves as a linear system; but it is still $\eta_a > \eta_a|_{\beta=0}$;
- for $\beta \geqslant \beta_c$ the impact does not occur and therefore the system behaves as a linear system; also $\eta_a < \eta_a|_{\beta=0}$ (this frequency range is highlighted with a green area in Fig. 7 and with a horizontal green line in Fig. 8a).

For $\delta_0 = \delta_{0c}$, (see also in Fig. 8c), $\beta_1 = 0$ and it is $\beta_1 = \beta_c = \sqrt{2}$ (the blue and green curves in Fig. 7 intersect and the cyan circle and green triangle in Fig. 8b overlap). Consequently:

- for $0 \leq \beta < \sqrt{2}$ the impact definitely occurs and it is $\eta_a > \eta_a|_{\beta=0}$;
- for $\beta \geq \sqrt{2}$ the impact does not occur and therefore the system behaver as a linear system; moreover, $\eta_a < \eta_a|_{\beta=0}$ (this frequency range is highlighted with a green area in Fig. 7 and with a horizontal green line in Fig. 8b).

For $0 < \delta_0 \leq \delta_{0c}$, (see also Fig. 8c, corresponding to $\delta_0 = 0.03$), $\beta_1 > 0$ and $\beta_c > \sqrt{2}$ and, furthermore, $\beta_2 > \beta_c$. Consequently:

- for $0 \leq \beta < \beta_c$ the impact definitely occurs. Compared to the linear case (FF), when impact occurs, for $\sqrt{2} \leq \beta < \beta_c$, it is $\eta_a > \eta_a|_{\beta=0}$. The amplitude of this frequency range, highlighted with a yellow area in Fig. 7 and with a horizontal yellow line in Fig. 8c, increases as δ_0 decreases;
- for $\beta_c < \beta \leq \beta_2$ the impact still occurs, but now it is $\eta_a < \eta_a|_{\beta=0}$, which means that the amplitude of the mass acceleration is lower than the amplitude of the ground acceleration, but is still higher than the acceleration under FF. The amplitude of this frequency range, highlighted with a magenta area in Fig. 7 and with a horizontal magenta line in Fig. 8c, increases as δ_0 decreases;
- for $\beta > \beta_2$ the impact does not occur and it is $\eta_a < \eta_a|_{\beta=0}$, and thus the system behaves as a linear system (this frequency interval is highlighted with a green area in Fig. 7 and a horizontal green line in Fig. 8c).

For $\delta_0 = 0$(see also Fig. 8d), impact occurs for every value of β and β_c reaches its maximum value ($\beta_c \simeq 3$). Consequently:

- for $0 \leq \beta < \beta_c$ the impact definitely occurs. Compared to the linear case (FF), when impact occurs, for $\sqrt{2} \leq \beta < \beta_c$ (frequency range highlighted in yellow), it is $\eta_a > \eta_a|_{\beta=0}$;
- for $\beta \geq \beta_c$ the impact still occurs, but it is $\eta_a < \eta_a|_{\beta=0}$, which means that the amplitude of the mass acceleration is lower than the amplitude of the ground acceleration, but is still higher than the acceleration under FF (frequency range highlighted in magenta).

Comparing PRCs in FF (black curves) and those associated with the occurrence of impact (red curves), it is observed that the V-IISs intervene on response (of both displacement and acceleration) selectively, introducing energy dissipation in a limited range of β, between β_1 and β_2, for each δ_0, where impact occurs. If $\delta_0 \geq \delta_{0c}$, only the positive effects of energy dissipation in the non-isolation range (reduction of the response of displacement and acceleration) are observed, without changing the response in isolation range. When, on the other hand, values of δ_0

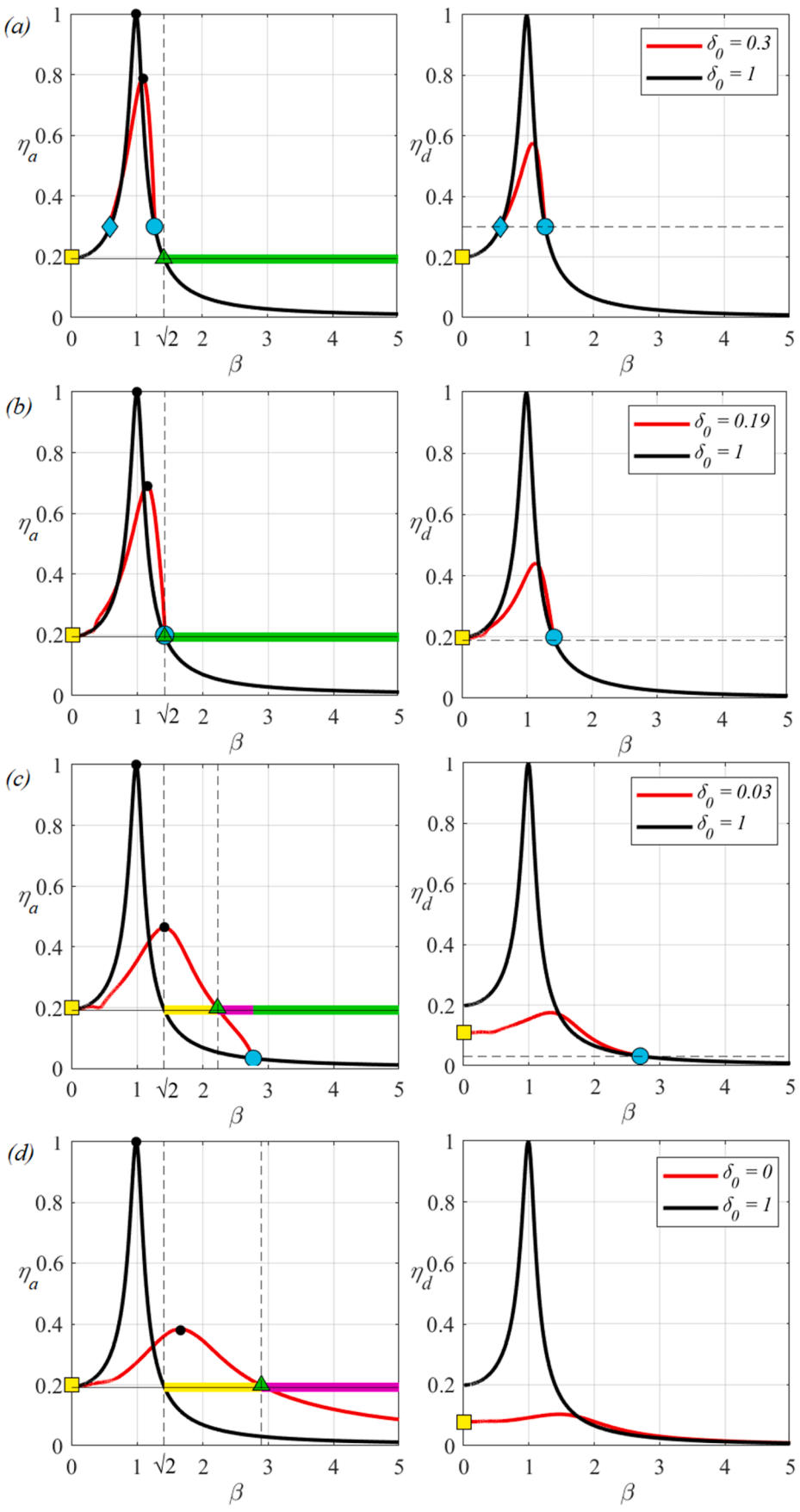

(caption on next page)

Fig. 8. PRCs of acceleration η_a, on the left, and displacement η_d, on the right, for different gap δ_0: *(a)* $\delta_0 = 0.3$, *(b)* $\delta_0 = 0.19$, *(c)* $\delta_0 = 0.03$, *(d)* $\delta_0 = 0$. Black line represents free-flight condition, red line represents the condition with optimal bumpers and for δ_0 fixed; The colored symbols represent the location of the characteristic β values (cyan diamond β_1; cyan circle β_2; black circle β_R; green triangle β_c) and the values of η_a and η_d for $\beta = 0$ (yellow squares). Finally, the colored lines represent different β ranges, that are obtained for $\beta > \sqrt{2}$: green line, η_a is lower than acceleration amplitude of the ground and equal to η_a in FF condition; magenta line, η_a is smaller than acceleration amplitude of the ground, but larger than η_a in FF condition; yellow line, η_a is greater than acceleration amplitude of the ground and than η_a in FF condition. (For interpretation of the references to color in this figure legend, the reader is referred to the web version of this article.)

smaller than δ_{0c} are selected, there begins to be a reduction in the isolation range, as well as a greater reduction in the maximum response values, compared with FF. Therefore, the best solution turns out to be the selection of a δ_0 such that β_2 is close to, but at the same time lower than, the isolation frequency β_I of the system, so that a good reduction in response, both in acceleration and displacement, is observed, while leaving the response for $\beta = \beta_I$ unchanged, compared to FF.

Form the PRCs of displacement also we observe the benefits that V-IISs can bring on the static displacement $q_{st} = u_{st}/u^*$. When $\delta_0 \geq \delta_0^* (\delta_0^* \simeq \delta_{0c})$, the static displacement is unchanged with respect to free flight; choosing $\delta_0 < \delta_0^*$, however, results in a reduction of q_{st}. In Fig. 9a, to highlight the effect of V-IISs on q_{st}, the trend of static displacement q_{st} as a function of δ_0 is shown.

From Fig. 9a it is observed that for values $\delta_0^* \leq \delta_0 \leq 1$, q_{st} is independent of δ_0 resulting equal to the FF ($q_{st} \simeq 0.199$). When $0 \leq \delta_0 < \delta_0^*$, q_{st} decreases as δ_0 decreases assuming the minimum value at $\delta_0 = 0$, which is equal to $q_{st} \simeq 0.08$. The dependence of the static displacement on the isolation frequency β_I of the system is not seen because of the way the equations were normalized, and the dimensionless static displacement q_{st} is defined. To highlight this dependence, a new dimensionless parameter representing the static displacement, $q_{st}^* = u_{st}/D_G$, where D_G is the peak ground displacement, is introduced as done in Section 2. Fig. 9b shown some representative curves of given values of q_{st}^* (2, 4, 9, 16) as a function of the design parameters δ_0 and β_I of the system; the range of interest is that of isolation, highlighted in green in Fig. 9b, related to $\beta > \sqrt{2}$. For $\delta_0^* \leq \delta_0 \leq 1$ values, q_{st}^* is independent of δ_0 and takes on larger values as β_I increases, while for $0 \leq \delta_0 < \delta_0^*$, to obtain fixed values of q_{st}^*, reducing δ_0 allows the system isolation frequencies β_I to be used at higher frequencies. From Fig. 9b, the static displacement q_{st}^* can thus be read, once the parameters of isolation frequency β_I and gap δ_0 are assigned. The curve for β_2 has also been plotted in this graph: the area to the right of this curve represents the domain of parameter pairs δ_0, β_I in which the V-IIS reports the same dynamic response in the isolation zone as a linear system designed with the same β_I. Therefore, the values of $\delta_0 = \delta_0^*$ and $\beta_I = \beta_2$, represent outliers separating from good or poor V-IIS behavior.

From the analysis in Fig. 9, one can appreciate the benefits that an appropriate choice of parameter δ_0 gives in terms of static displacement of the system, compared to FF ($\delta_0 = 1$).

6. Results

This Section analyzes the numerical response of different Vibro-Impact Isolation systems (V-IISs), all defined by a damping ratio $\xi = 0.10$, each of which is characterized by a fixed value of δ_0 and a corresponding pair of values λ_{opt}, γ_{opt} of which λ_{opt} is obtained, for fixed δ_0, through the optimal curve (Fig. 6a), and successively γ_{opt}, is obtained through the optimality relationship (Eq.(7)). The responses represented are the dimensionless absolute acceleration (α, which is equivalent to the dimensionless total force of the system f_I) and the dimensionless relative displacement ($d = q$) of the mass, the dimensionless contact force (f_j, $j = R, L$) and the dimensionless displacement of the bumpers ($d_j = q_j + \delta_0$ with $j = R$, $d_j = q_j - \delta_0$ with $j = L$), as a function of time. Also represented are the normalized excursion of absolute acceleration $\eta_a = \Delta\alpha/\Delta\alpha_0$, the normalized excursion of relative mass displacement $\eta_d = \Delta d/\Delta d_0$, the normalized excursion of contact force $\eta_F = \Delta f_B/\Delta\alpha_0$, and the normalized excursion of bumper deformation $\eta_B = \Delta d_B/\Delta d_0$. These quantities are represented as a function of the frequency β, through the Pseudo-Resonance Cures (PRCs). PRCs were obtained with sweeps performed by applying the continuation technique, where the final values of the state variables (displacement and velocity) of the system are taken as initial conditions of the following analysis; the driving frequency is slightly changed as soon as the steady state is attained and a new stable solution is searched for. The excursion Δi (where $i = \alpha, d, f_B, d_B$) are calculated as the difference between the maximum and minimum values recorded at the steady-state of each frequency sub-interval. To calculate the excursion of contact force Δf_B and bumper deformation Δq_B, both bumpers are considered, specifically for maximum values the right bumper and for minimum values the left

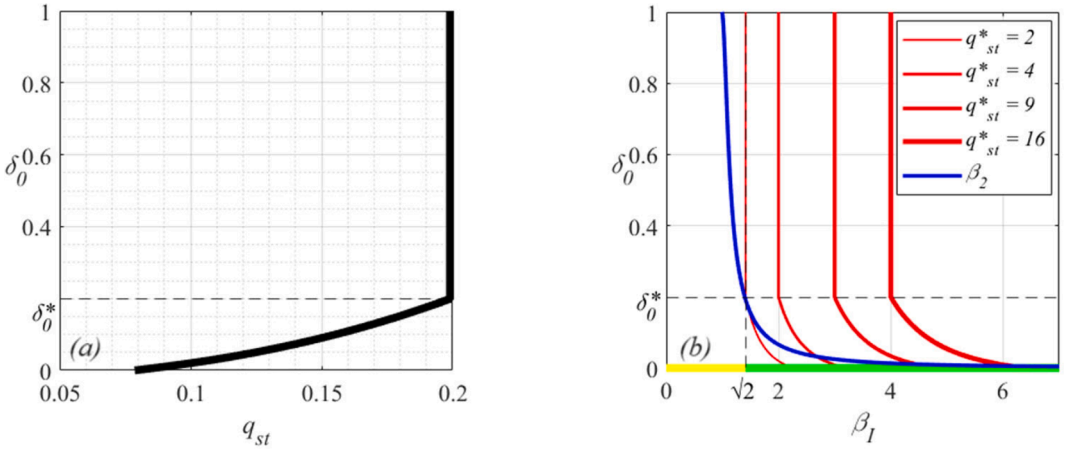

Fig. 9. In *(a)*, black line shows the trend of static displacement q_{st}, normalized with respect to the peak mass displacement in free-flight condition u^*, as a function of gap δ_0 and in *(b)*, red lines show the trend for four different values of static displacement q_{st}^* (2, 4, 9, 16; lower thickness means lower values), normalized with respect to peak ground displacement D_G, of isolation frequency β_I as a function of gap δ_0. This graph also shows the outliers β_2 (blue line), δ_0^* (dashed horizontal straight line) and $\beta = \sqrt{2}$ (dashed vertical straight line), the last separates the non-isolation range (yellow line) from the isolation range (green line). (For interpretation of the references to color in this figure legend, the reader is referred to the web version of this article.)

bumper. Normalization is done with respect to $\Delta\alpha_0$ and Δd_0, which indicate the maximum excursion of absolute acceleration, as well as total force, and relative displacement in free-flight condition FF, respectively.

Subsection 6.1 studies the steady-state response through the Pseudo-Resonance Curves (PRCs) in acceleration and displacement of the mass and in contact force and deformation of the bumpers, obtained for four different values of δ_0 and for FF; Subsection 6.2 studies the transient response through time histories and force–displacement cycles obtained by applying a harmonic action to the base with constant amplitude and time-varying frequency, for the same δ_0, comparing them with the FF.

The values of δ_0 examined are characteristic of four different cases: $\delta_0 = 0.3 > \delta_c \simeq \delta_0^*$; $\delta_0 = 0.19 \simeq \delta_{0c} \simeq \delta_0^*$; $\delta_0 = 0.03 < \delta_{0c} \simeq \delta_0^*$; $\delta_0 = 0$ mass boundary condition adjacent to bumpers. δ_{0c} indicates the value of δ_0 below which there starts to be a reduction of the isolation range; while δ_0^* indicates the value of δ_0 below which there starts to be a reduction of the static displacement.

6.1. Steady-state response analysis

Fig. 10a and 10b show PRCs of the dimensionless response quantities related to mass, acceleration η_a and displacement η_d, respectively. The black curves reproduce the transmissibility (Fig. 10a) and displacement response factor (Fig. 10b), given in Section 2, scaled with respect to their peak, respectively, for a system having $\xi = 0.1$ (free-flight condition FF, $\delta_0 = 1$). The red curves are related to four different values of δ_0 (the smaller the line thickness, the lower the reference δ_0). Depending on the different β ranges, different considerations can be made in terms of both acceleration and displacement.

As for the acceleration η_a (Fig. 10a):

- in the quasi-static response range, $\beta \ll 1$, the acceleration is found to be independent of δ_0 and has a value approximately equal to peak ground acceleration A_G;
- in the resonance range, the maximum acceleration of the mass encounters greater reduction as δ_0 decreases, compared with the FF; in fact, the absolute maximum is reduced, by 21% for $\delta_0 = 0.3$, by 31% for $\delta_0 = 0.19$, by 54% for $\delta_0 = 0.03$ and by 62% for $\delta_0 = 0$. In addition, along with a reduction in response, an enlargement of the resonance range is exhibited, that is an increase of the width of the range of β within which maximum mass acceleration is greater than peak ground acceleration;
- in the range straddling the resonance range and the isolation range, for values of $\beta < \beta_2$, η_a shows larger increases as δ_0 decreases relative to FF;

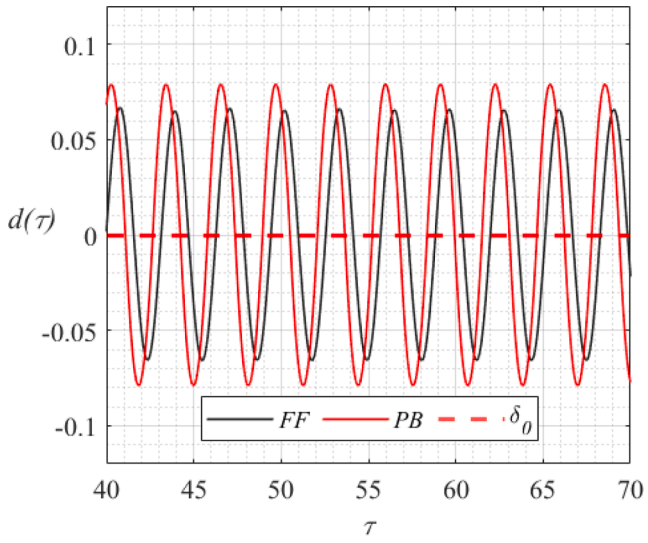

Fig. 11. Displacement time histories of displacement for a linear system (black line) and a V-IIS (red line); the systems have the same isolation frequency ($\beta = \beta_I = 2$) and the same damping ratio ($\xi = 0.1$), while the V-IIS also has a gap $\delta_0 = 0$. (For interpretation of the references to color in this figure legend, the reader is referred to the web version of this article.)

- for $\beta \geq \beta_2$ the red curves overlap with the black curve relative to FF, whereas for $\delta_0 = 0$ this overlap with the black curve does not occur, since the mass impacts the bumpers for any values of β (the β_2 frequency ratio beyond which the mass no longer impacts the bumpers tends to infinity).

As for the displacement η_d (Fig. 10b):

- in the quasi-static response range, the displacement does not change with respect to FF if $\delta_0 \geq \delta_0^*$, while if $\delta_0 < \delta_0^*$ it decreases as δ_0 decreases with respect to FF. The static displacement for $\delta_0 = 0.03$ shows a reduction of 45% and for $\delta_0 = 0$ shows a reduction of 61%, while for $\delta_0 = 0.3$ and $\delta_0 = 0.19$ it shows no change, with respect to FF;
- in the resonance range, as already for acceleration, the displacement exhibits greater reductions as δ_0 decreases, with respect to FF; in fact, the absolute maximum shows reductions of 42%, 56%, 82%, and 90% for $\delta_0 = 0.3, 0.19, 0.03,$ and 0, respectiely;

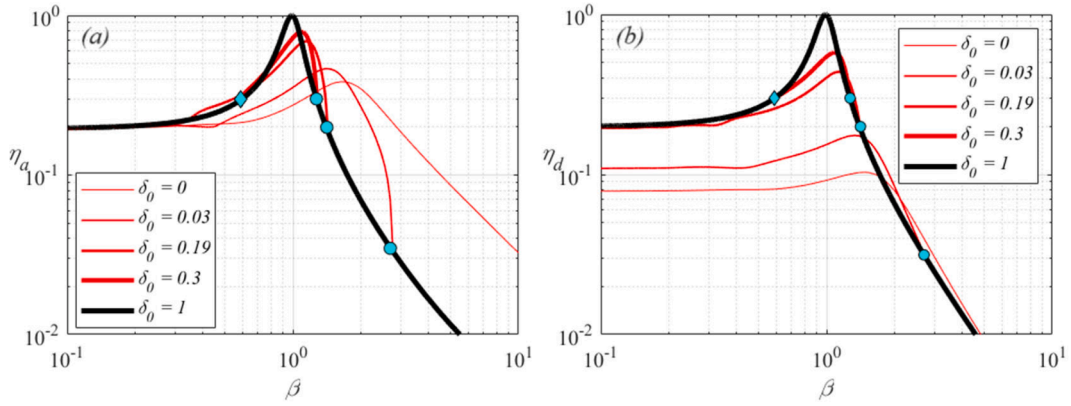

Fig. 10. PRCs of acceleration *(a)* and of displacement *(b)*: black lines are related to FF, red lines are related to four different values of δ_0 (0, 0.03, 0.19, 0.3; thinner line thickness means smaller values of δ_0). The cyan diamond and cyan circle represent the β_1 and β_2, respectively; for curves in which the value of β_1 is not reported it is because this is 0, while for those in which the value of β_2 is not reported (case of $\delta_0 = 0$) these tend to infinity. (For interpretation of the references to color in this figure legend, the reader is referred to the web version of this article.)

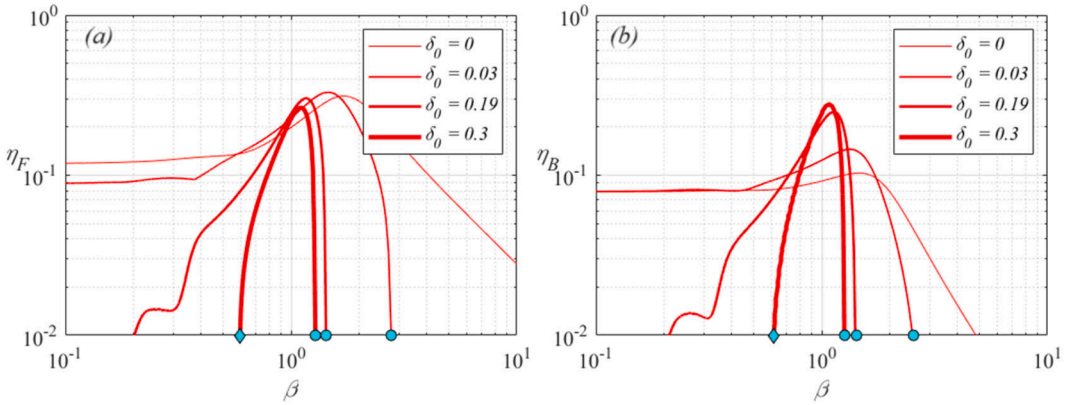

Fig. 12. PRCs of contact force *(a)* and of bumper deformation *(b)*: red lines are related to four different values of δ_0 (0, 0.03, 0.19, 0.3; thinner line thickness means smaller values of δ_0). The cyan diamond and cyan circle represent the β_1 and β_2, respectively; for curves in which the value of β_1 is not reported it is because this is 0, while for those in which the value of β_2 is not reported (case of $\delta_0 = 0$) these tend to infinity. (For interpretation of the references to color in this figure legend, the reader is referred to the web version of this article.)

- in the β ranges straddling the resonance range and the isolation range, each of these ranges relative to a δ_0, the response obtained with V-IISs is greater than the response in FF (Fig. 11);
- for $\beta \geq \beta_2$ the red curves overlap with the black curve related to FF, whereas, as already for acceleration, the curve corresponding to $\delta_0 = 0$ does not overlap with black curve, since the mass impacts with the bumpers for any value of β.

Fig. 12a and 12b show PRCs of dimensionless response quantities related to the bumper, contact force η_F and deformation η_B. The red curves are related to four different values of δ_0 (the thinner the line thickness, the smaller the reference value of δ_0). Based on the different β ranges, different considerations can be made about the performance of these curves in terms of both contact force and bumper deformation.

As for the contact force η_F (Fig. 12a):

- in the quasi-static response range, with $\beta < \beta_1$ (remembering that for $\delta_0 \leq \delta_0^* \beta_1 = 0$), the contact force turns out to be zero until $\beta = \beta_1$, relative to different δ_0 investigated, is reached. Thereafter, when $\beta \geq \beta_1$ the contact force decreases as δ_0 increases;
- in the resonance range, the contact force reaches absolute maxima that converge, for each δ_0 investigated, at about 0.3;
- in the range following the resonance range, the contact force returns to increasing values as δ_0 decreases.

As for the bumper deformation η_B (Fig. 12b):

- in the quasi-static response range, when $\beta < \beta_1$ (always remembering that for $\delta_0 \leq \delta_0^* \beta_1 = 0$), the deformation turns out to be zeros until $\beta = \beta_1$, relative to different δ_0 investigated, is reached. Thereafter, with $\beta \geq \beta_1$ the bumper deformation decreases as δ_0 increases;
- in the resonance range, the deformation shows absolute maximum values, which become greater as δ_0 increases; in fact, the absolute maximum for $\delta_0 = 0.3$ is 0.28,for $\delta_0 = 0.19$ is 0.25, for $\delta_0 = 0.03$ is 0.15, and for $\delta_0 = 0$ is 0.10;
- in the range following the resonance range, the bumper deformation reverts to increasing values as δ_0 decreases.

For each δ_0, both η_F and η_B, assume zero value for $\beta \leq \beta_1$ and for $\beta \geq \beta_2$, as there is no contact between mass and bumper.

Comparing the responses, reported in the PRCs, obtained with the V-IIS (red curves) and the linear system without impact (black curves) at the same frequency, different observations can be drawn depending on the β range we are in. Around the resonant frequency of the linear system, acceleration (Fig. 10a) and displacement (Fig. 10b) responses obtained with the V-IIS are always lower than that obtained with the linear system; moreover, the reduction of the response, compared with the linear system, is greater by reducing the δ_0 parameter. For these β values, however, both contact force (Fig. 12a) and bumper deformation (Fig. 12b) show the maximum response values, which, as far as contact force is concerned, are at an almost identical value for each value of the δ_0 parameter, while, as far as deformation is concerned, the maximum response values decrease in intensity as the δ_0 parameter decreases. In the isolation range, on the other hand, the acceleration and displacement responses report greater, or at most equal, values in the V-IIS system than in the linear system, and are the greater the lower the δ_0 parameter. In this range, contact force and bumper deformation exhibit modest values.

From the analysis of these curves (Figs. 10 and 12), it is also observed that the lowest peak acceleration and displacement values and the lowest static displacement value are exhibited at $\delta_0 = 0$; however, for $\beta > \beta_c$ (with β_c defined as the frequency ratio over which the acceleration transmitted to the mass is lower than the ground acceleration, i.e., β of beginning isolation), $\delta_0 = 0$ is characterized by an always greater response than the free-flight case and the cases corresponding to larger gap values.

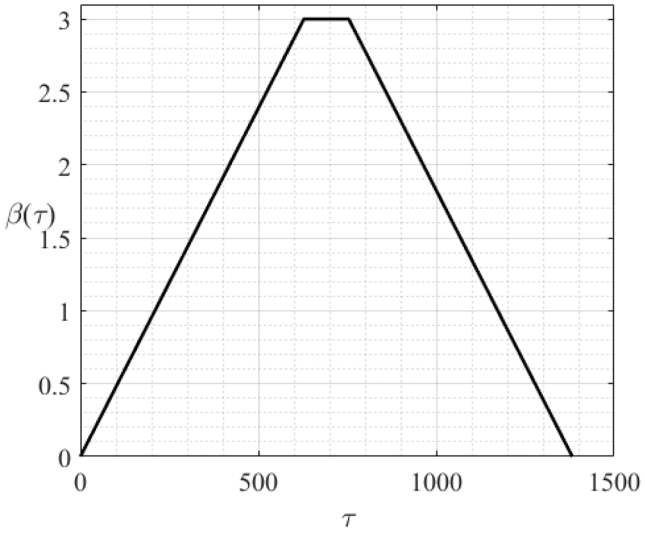

Fig. 13. Trend of the frequency harmonic excitation to the base as function of the dimensionless time τ; the dimensionless frequency β of the harmonic excitation is defined as the ratio of harmonic excitation frequency to system frequency.

To limit the reduction in the benefits of the isolation range, compared with the linear case, it would be appropriate to consider greater values of δ_0, but still small, accepting greater peaks of both acceleration and displacement, bumper deformation and static displacement.

6.2. Transient response analysis

The time histories and force–displacement cycles, show in this Subsection, refer to the application of harmonic excitation to the base of constant amplitude and time varying frequency. The law of frequency variation is shown in Fig. 13. This is characterized by 3 traits: in the first trait the frequency of the harmonic excitation, represented by the dimensionless parameter β, varies linearly from 0 to the isolation

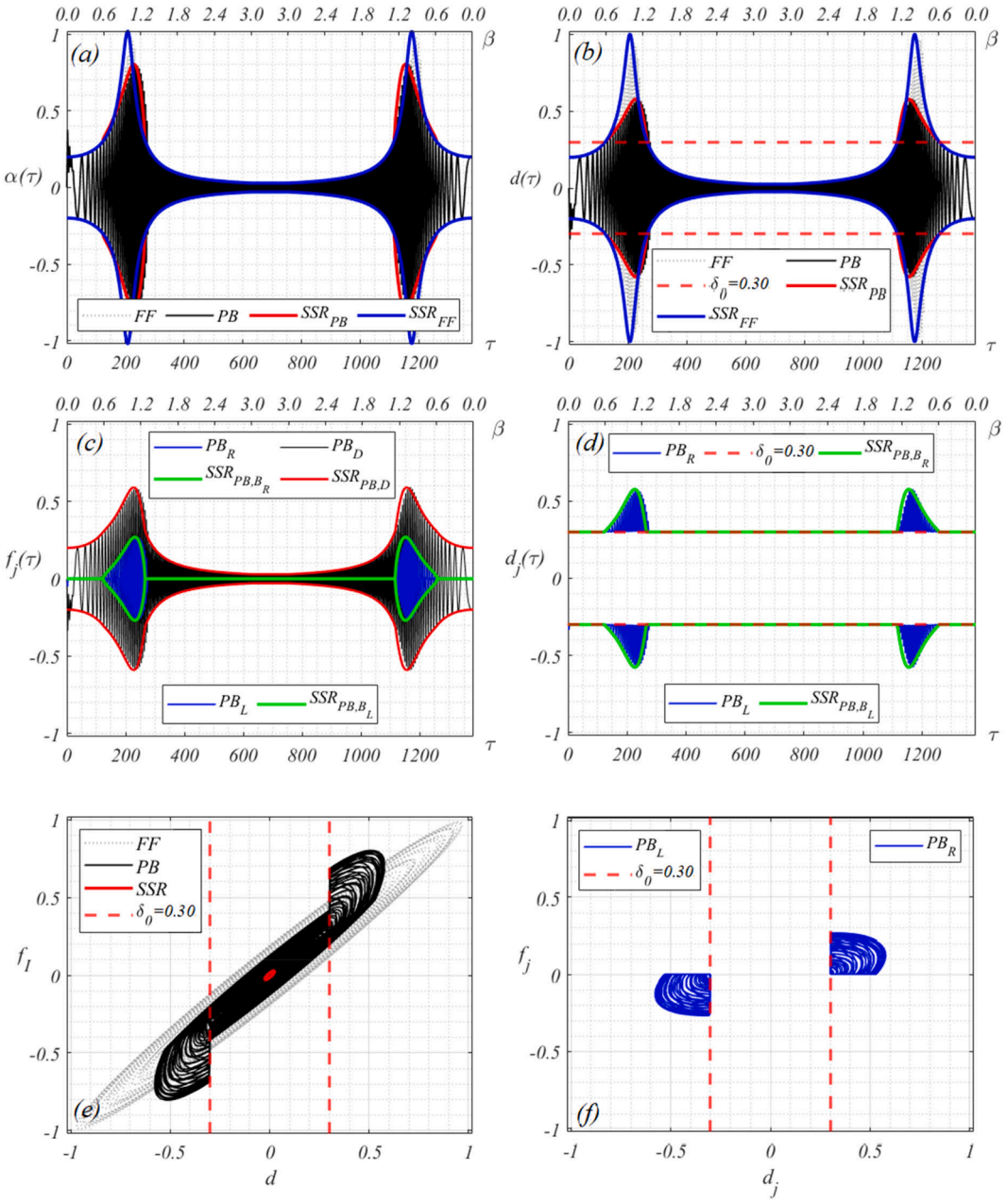

Fig. 14. In the first row, time histories of dimensionless absolute acceleration of the mass *(a)* and dimensionless relative displacement of the mass *(b)*: the gray dotted line is related to free-flight condition *FF*, the black line is related to impact condition with bumpers design in optimality *PB*, the blue line and red line represent the Steady-State Response values for the β in which the system is at each instant of time τ, in free flight SSR_{FF} and impact SSR_{PB} condition, respectively. In the second row, time histories of dimensionless contact force of the bumpers *(c)* and dimensionless deformation of the bumpers *(d)* in impact condition with optimal bumpers: the black line is related to damper PB_D; the blue lines are related to right bumper PB_R and left bumper PB_L; the red line, related to the damper $SSR_{PB,D}$, and green line, related to the bumper $SSR_{PB,j}$ (j=R right bumper, j=L left bumper), represent the Steady-State Response values for the β in which the system is at each instant of time τ. In the last row, force-displacement cycles of system *(e)* and bumpers *(f)*: the gray dotted line is related of free-flight condition *FF*, the black line is related to impact condition with bumpers design in optimality *PB*, the blue lines are related to right bumper PB_R and left bumper PB_L, the red line represent the system response when the frequency force is constant. In figures *(b) (d) (e)* and *(f)*, the red dashed lines represent the dimensionless gap that characterizes the V-IIS which is equal to 0.3 and, the system presents $\xi = 0.1$. All the graphs in the figure have a second (upper) x-axis that defines the β to which the system is subjected during the application of harmonic excitation. (For interpretation of the references to color in this figure legend, the reader is referred to the web version of this article.)

frequency value $\beta_I = 3$ taking a dimensionless time $\tau_1 = 200\pi$; in the second trait the frequency takes on a constant value such that $\beta = \beta_I = 3$, until $\tau_2 = 240\pi$ is reached; in this trait the system response reaches steady-state (SS); finally in the last trait the frequency takes on a linearly decreasing trend going from $\beta = \beta_I = 3$ to $\beta = 0$, a value reached at dimensionless time $\tau_3 = 440\pi$.

The results shown in Figs. 14–17 refer to four different values of δ_0 (0.3, 0.19, 0.03, 0) that are compared with the free-flight condition FF. The first row of these figures refers to the characteristic quantities of the mass, dimensionless absolute acceleration α on the left *(a)* and dimensionless relative displacement d on the right *(b)*; the second row reports the bumper quantities, on the left dimensionless contact force f_j, with $j = R,L$, *(c)* and on right dimensionless bumper displacement d_j, with $j = R, L$, *(d)*; finally, the third row reports the force–displacement cycles, on the left inertia force vs. mass displacement $f_I - d$ *(e)* and on the right contact force vs. bumper deformation $f_j - d_j$, with $j = R, L$, *(f)*. In

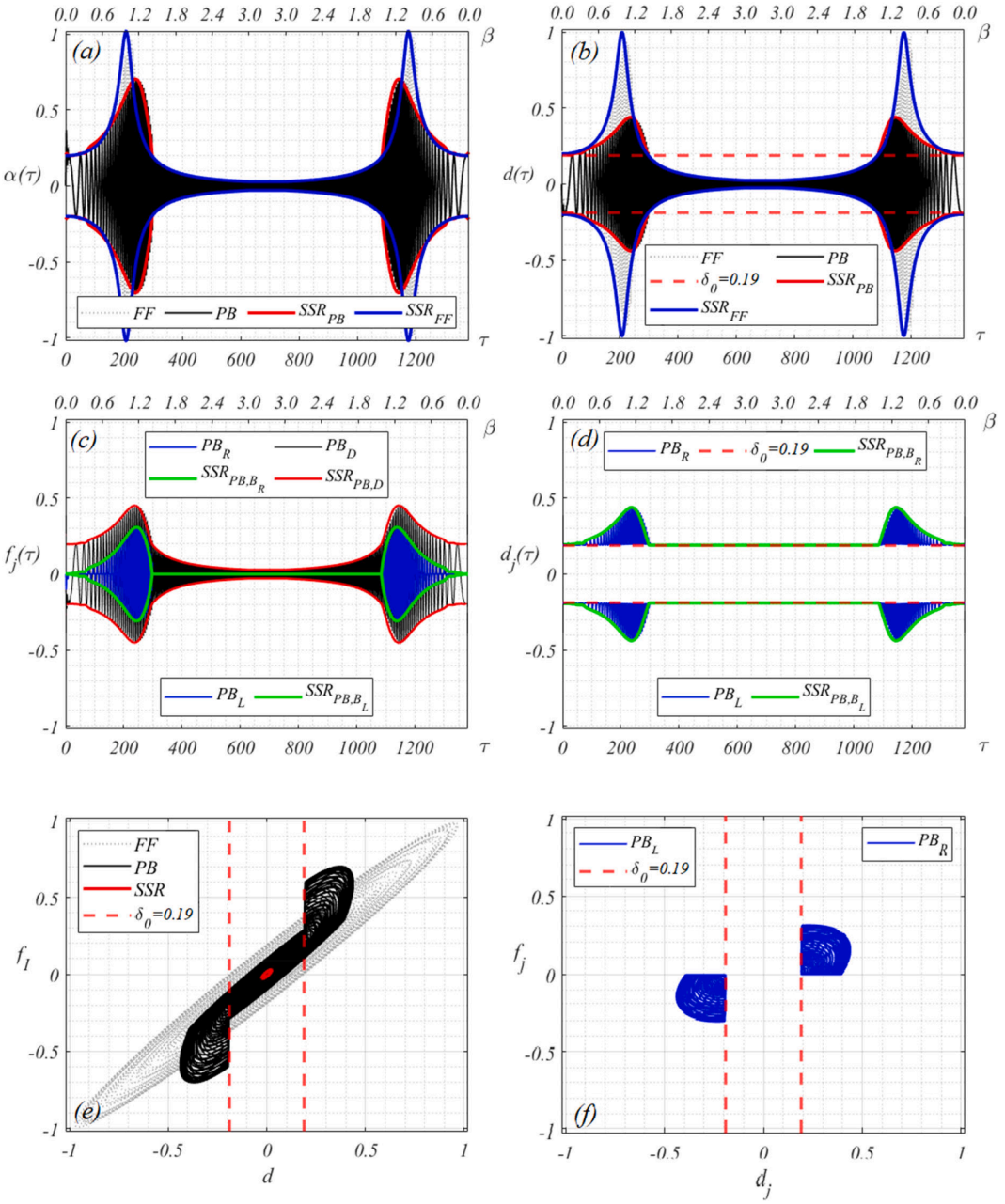

Fig. 15. In the first row, time histories of dimensionless absolute acceleration of the mass *(a)* and dimensionless relative displacement of the mass *(b)*: the gray dotted line is related to free-flight condition *FF*, the black line is related to impact condition with bumpers design in optimality *PB*, the blue line and red line represent the Steady-State Response values for the β in which the system is at each instant of time τ, in free flight SSR_{FF} and impact SSR_{PB} condition, respectively. In the second row, time histories of dimensionless contact force of the bumpers *(c)* and dimensionless deformation of the bumpers *(d)* in impact condition with optimal bumpers: the black line is related to damper PB_D; the blue lines are related to right bumper PB_R and left bumper PB_L; the red line, related to the damper $SSR_{PB,D}$, and green line, related to the bumper $SSR_{PB,j}$ (j=R right bumper, j=L left bumper), represent the Steady-State Response values for the β in which the system is at each instant of time τ. In the last row, force-displacement cycles of system *(e)* and bumpers *(f)*: the gray dotted line is related of free-flight condition *FF*, the black line is related to impact condition with bumpers design in optimality *PB*, the blue lines are related to right bumper PB_R and left bumper PB_L, the red line represent the system response when the frequency force is constant. In figures *(b) (d) (e)* and *(f)*, the red dashed lines represent the dimensionless gap that characterizes the V-IIS which is equal to 0.19 and the system presents $\xi = 0.1$. All the graphs in the figure have a second (upper) x-axis that defines the β to which the system is subjected during the application of harmonic excitation. (For interpretation of the references to color in this figure legend, the reader is referred to the web version of this article.)

Figs. 14–17a,b,e the trends of the mass quantities, obtained by impact, are shown with a continuous black line (*PB*, Preferable Bumper), and those without impact with a dashed black line (*FF*); in Figs. 14–17c,d,f the bumper quantities are shown with a continuous blue line (PB_R, right bumper, and PB_L, left bumper).

Also in the same Figs. 14–17, the curves representing the Steady-State Response (*SSR*) values of the mass responses (displacement and acceleration) and of the bumpers responses (contact force and deformation), for each value of β in which the system is located during the application of the harmonic excitation to the base, are then shown, both for the condition with impact (red curve, Figs. 14–17a,b,c, and green curve, Figs. 14–17c,d, denoted by SSR_{PB} and $SSR_{PB,i}$, where $i = R$ refers to the right bumper, $i = L$ refers to the left bumper, and $i = D$ refers to the damper) and for the FF (blue curve, SSR_{FF}, Figs. 14–17a,b).

The graphs representing the quantities as a function of time (Figs. 14–17a,b,c,d), have an additional axis at the top showing the β

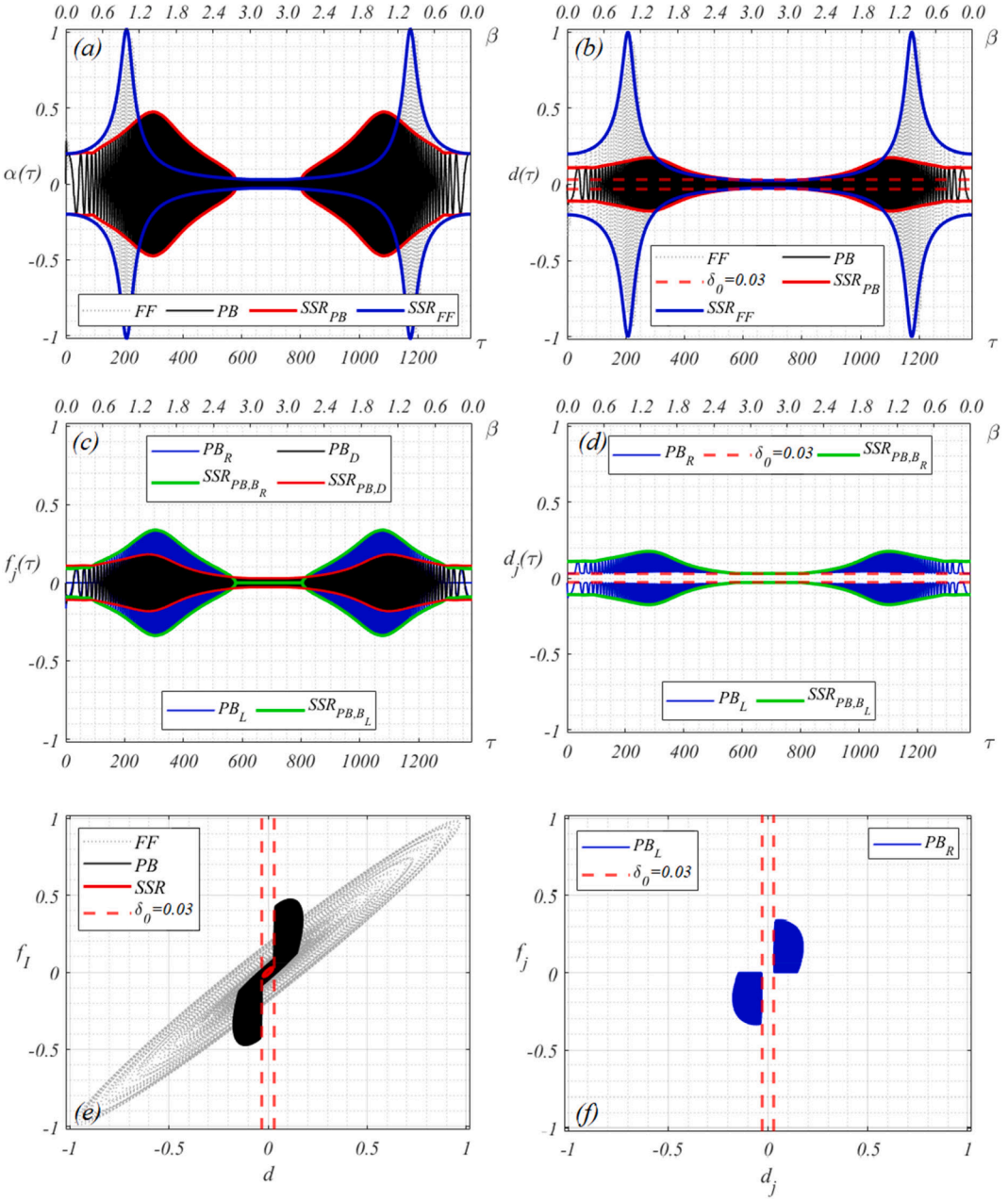

Fig. 16. In the first row, time histories of dimensionless absolute acceleration of the mass *(a)* and dimensionless relative displacement of the mass *(b)*: the gray dotted line is related to free-flight condition *FF*, the black line is related to impact condition with bumpers design in optimality *PB*, the blue line and red line represent the Steady-State Response values for the β in which the system is at each instant of time τ, in free flight SSR_{FF} and impact SSR_{PB} condition, respectively. In the second row, time histories of dimensionless contact force of the bumpers *(c)* and dimensionless deformation of the bumpers *(d)* in impact condition with optimal bumpers: the black line is related to damper PB_D; the blue lines are related to right bumper PB_R and left bumper PB_L; the red line, related to the damper $SSR_{PB,D}$, and green line, related to the bumper $SSR_{PB,j}$ (j=R right bumper, j=L left bumper), represent the Steady-State Response values for the β in which the system is at each instant of time τ. In the last row, force-displacement cycles of system *(e)* and bumpers *(f)*: the gray dotted line is related of free-flight condition *FF*, the black line is related to impact condition with bumpers design in optimality *PB*, the blue lines are related to right bumper PB_R and left bumper PB_L, the red line represent the system response when the frequency force is constant. In figures *(b) (d) (e)* and *(f)*, the red dashed lines represent the dimensionless gap that characterizes the V-IIS which is equal to 0.03 and the system presents $\xi = 0.1$. All the graphs in the figure have a second (upper) x-axis that defines the β to which the system is subjected during the application of harmonic excitation. (For interpretation of the references to color in this figure legend, the reader is referred to the web version of this article.)

value of the system for each instant of time τ.

Fig. 14 shows the time response of the system quantities with a dimensionless gap $\delta_0 = 0.3$. In Fig. 14a, a 15% reduction in maximum acceleration is observed in the V-IIS, with respect to FF. These maxima occur near values of the frequency ratio β close to unity, that is, when the harmonic excitation frequency is close to the system frequency. For values of β for which impact does not occur ($\beta \leq \beta_1$ and $\beta \geq \beta_2$, remembering that β_1 and β_2 represent the lower and upper extremes, respectively, of the frequency range in which, for each value of δ_0, impact definitely occurs), the curves for the condition with and without impact are overlapping; on the other hand, in the range $\beta_1 < \beta < \beta_2$, there is initially a reduction in the response for $\beta \simeq \beta_R$ (indicating, for each δ_0, the value of the resonance frequency ratio), are then an increase, with respect to FF. Fig. 14b shows a 37% reduction in the maximum displacement in V-IIS, with respect to FF. These maxima always occur for β close to unity. For the values of β for which the impact

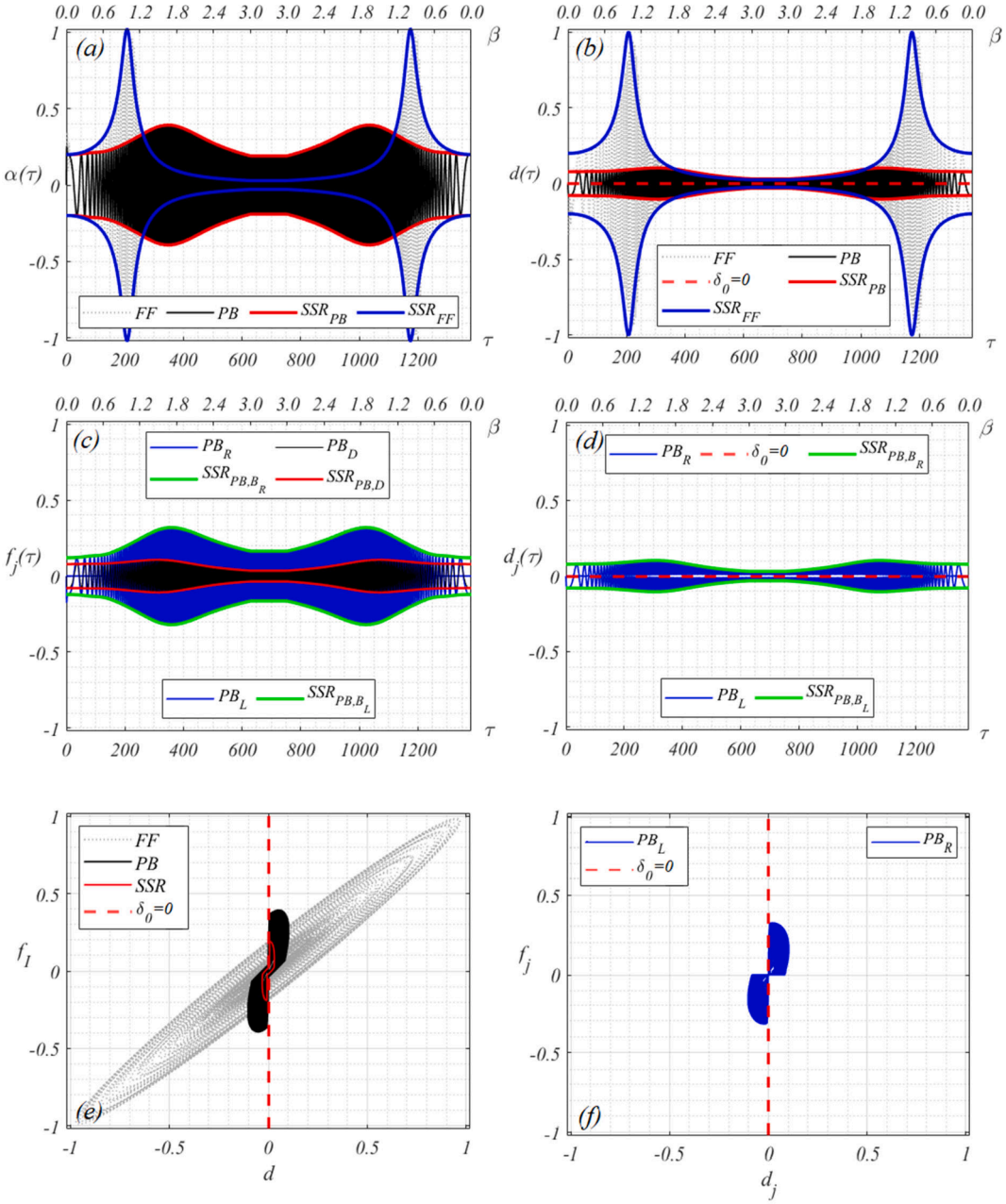

Fig. 17. In the first row, time histories of dimensionless absolute acceleration of the mass *(a)* and dimensionless relative displacement of the mass *(b)*: the gray dotted line is related to free-flight condition *FF*, the black line is related to impact condition with bumpers design in optimality *PB*, the blue line and red line represent the Steady-State Response values for the β in which the system is at each instant of time τ, in free flight SSR_{FF} and impact SSR_{PB} condition, respectively. In the second row, time histories of dimensionless contact force of the bumpers *(c)* and dimensionless deformation of the bumpers *(d)* in impact condition with optimal bumpers: the black line is related to damper PB_D; the blue lines are related to right bumper PB_R and left bumper PB_L; the red line, related to the damper $SSR_{PB,D}$, and green line, related to the bumper $SSR_{PB,j}$ (j=R right bumper, j=L left bumper), represent the Steady-State Response values for the β in which the system is at each instant of time τ. In the last row, force-displacement cycles of system *(e)* and bumpers *(f)*: the gray dotted line is related of free-flight condition *FF*, the black line is related to impact condition with bumpers design in optimality *PB*, the blue lines are related to right bumper PB_R and left bumper PB_L, the red line represent the system response when the frequency force is constant. In figures *(b) (d) (e)* and *(f)*, the red dashed lines represent the dimensionless gap that characterizes the V-IIS which is equal to zero and the system presents $\xi = 0.1$. All the graphs in the figure have a second (upper) x-axis that defines the β to which the system is subjected during the application of harmonic excitation. (For interpretation of the references to color in this figure legend, the reader is referred to the web version of this article.)

does not occurs, $\beta \leq \beta_1$ and $\beta \geq \beta_2$, the curves for the condition with and without impact, are overlapping; however, in the range $\beta_1 < \beta < \beta_2$, there is initially a reduction in the response for $\beta \simeq \beta_R$, and then a increase, with respect to FF. Fig. 14c shows the trend of dimensionless contact force (in blue), which is compared with the trend of dimensionless damper force (in black), as a function of dimensionless time τ. These two quantities have their maximum values near β_R of 0.27 and 0.60, respectively. The damper force, for $0 < \beta < \beta_R$, reports increasing values, while for $\beta_R < \beta < \beta_I$, it takes on decreasing values; as for the contact force, on the other hand, these ranges, $0 < \beta < \beta_R$ and $\beta_R < \beta < \beta_I$, reduce to $\beta_1 < \beta < \beta_R$, where the response increases in intensity, and to $\beta_R < \beta < \beta_2$, where it decreases; for all other values of β, the contact force is zero. The dimensionless displacement of the bumpers (Fig. 14d) reports the same trend as the contact force: between $\beta_1 < \beta < \beta_R$, the response increases, and between $\beta_R < \beta < \beta_2$, it shows a decreasing trend; for all other values of β, it turns out to be constant and equal to δ_0 (0.30). The maximum, in the absolute value, of the bumpers displacement occurs, therefore, for $\beta = \beta_R$, and is equal to 0.70. The displacement cycles, shown in Fig. 16e and 16f, summarize what has already been said, highlighting the reduction in the displacement and total force of the system through the use of V-IIS in the face of an increase in the contact force and displacement, as well as in the deformation, of the bumpers. Finally, it should be pointed out that the V-IIS designed with this value of the parameter δ_0 (equal to 0.3), shows a static displacement q^*_{st} equal to that of a linear isolated system and equal to 9. The static displacement does not undergo a reduction because δ_0 is greater than $\delta^*_0 = 0.19$.

Fig. 15 shows the time response of the system quantities with $\delta_0 = \delta_{0c} \simeq 0.19$, with δ_{0c} representing the value of the gap below which the value of the frequency ratio of start of isolation β_c begins to assume values greater than $\sqrt{2}$. The trends of the quantities investigated are similar to those observed in Fig. 14. Thus, 25% reduction of the maximum acceleration in V-IIS, with respect to FF, is observed in Fig. 15a. Fig. 15b shows a 50% reduction of maximum displacement in the V-IIS, with respect to FF. the contact force and damper force, shown in Fig. 15c, have the maximum values near β_R of 0.30 and 0.45, respectively. The absolute maximum value of the bumpers displacement (Fig. 15d) turns out to be 0.45. Finally, it should be pointed out that the V-IIS designed with this value of the parameter δ_0 (equal to 0.19), shows a static displacement q^*_{st} equal to that of a linear isolated system and equal to 9. The static displacement does not undergo a reduction because δ_0 is equal to the outlier value $\delta^*_0 = 0.19$.

Fig. 16 shows the time responses of the system quantities with $\delta_0 = 0.03$. The trends of the investigated quantities are similar to those observed in Fig. 15. Thus, a 50% reduction of maximum acceleration in V-IIS is observed in Fig. 16a, with respect to FF. Fig. 16b shows a 77% reduction of maximum displacement obtained with V-IIS, with respect to FF. The contact force and damper force, shown in Fig. 16c, have the maximum values near β_R of 0.35 and 0.20, respectively. The absolute maximum value of the bumpers displacement (Fig. 16d) turns out to be 0.20. Finally, it should be pointed out that the V-IIS designed with this value of the parameter δ_0 (equal to 0.03), shows a reduction in static displacement q^*_{st} compared to the linear isolated system, as δ_0 is smaller than $\delta^*_0 = 0.19$. In fact, the static displacement turns out to be $q^*_{st} = 5$, thus undergoing a 44% reduction compared to FF (where $q^*_{st} = 9$).

Fig. 17shows the time response of the system quantities with $\delta_0 = 0$. The difference with the previous cases is due to the intensity of the maximum values of investigated quantities, in absolute value, and the values at Steady-State, i.e., in the trait between τ_1 and τ_2 where a constant frequency harmonic excitation is applied. In Fig. 17a, the greatest reduction, 55 %, of the maximum acceleration obtained by V-IIS, with respect to FF is exhibited. Fig. 17b also reports a greater reduction than the other scenarios, of 85%, of the maximum displacement obtained by V-IIS, with respect to FF. The contact force and damper force, shown in Fig. 17c, have the maximum values near β_R of 0.32 and 0.11, respectively. The absolute maximum value of the bumpers displacement (Fig. 17c) turns out to be 0.11. As for steady-state response, on the other hand, which is reached for values of $\beta = \beta_I$ relative to the constant trait of the frequency function of the harmonic excitation (horizontal trait in Fig. 13), for the case $\delta_0 = 0$, since $\beta_I < \beta_2(\delta_0 = 0)$ there is impact between mass and bumpers; therefore, the greater values of response in both absolute acceleration and relative displacement are reported than for the other scenarios in which the system response is equal to that in FF, since for these δ_0, $\beta_I > \beta_2|_{\delta_0=0.03,0.19,0.3}$. In fact, the acceleration, when $\beta = \beta_I$ in the case of $\delta_0 = 0$, shows an increase of 530%, whereas the displacement shows an increase of 20%, with respect to FF. The contact force and damper force, shown in Fig. 17c, have the maximum values near β_R of 0.32 and 0.11, respectively. The absolute maximum value of the bumpers displacement (Fig. 17c) turns out to be 0.11. Finally, it should be pointed out that the V-IIS designed with $\delta_0 = 0$, shows the greatest reduction in static displacement q^*_{st} compared to the linear isolated system. In fact, the static displacement turns out to be $q^*_{st} = 3.5$, thus undergoing a 61% reduction compared to FF (where $q^*_{st} = 9$).

The gradient of the curve representing the variation in the frequency of harmonic excitation, summarized by the parameter τ_1, was also subject to preliminary analysis. However, this parameter showed no influence on the maximum response values, except on the number of impacts: the lower τ_1, the higher the gradient of the line and the fewer impacts; conversely, the higher τ_1, the lower the gradient and the higher the number of impacts. Therefore, these results bring out the influence of two parameters, β_I and δ_0, on the response of V-IIS. The choice of a $\beta_I > \beta_2(\delta_0)$ allows to obtain benefits in the resonance range, and thus in the reduction of the maximum amplification of the response, and not to change the response in the isolation range, remembering, however, that as β_I increases, the static displacement increases; smaller values of δ_0 allow to reduce not only the maximum dynamic amplification of the response, but also the static displacement, if $\delta_0 < \delta^*_0$, remembering, however, that small values of δ_0 correspond to large values of β_2. Therefore, the choice of these two parameters β_I and δ_0 must be made together, going through the evaluation of the two outlier values δ^*_0 and $\beta_2(\delta_0)$ that influence the operation of V-IIS and thus the choice of the two parameters.

Another purpose of transient analysis with time histories is to assess whether or not PRCs, obtained by sweeps performed with the continuation technique, succeed in reproducing the response of the system to the transient. Therefore, being able to say that the steady-state values, for each β in which the system is located during the application of the harmonic excitation in Fig. 13, reproduce an envelope of the maximum values of the quantities of both mass acceleration and displacement and bumper deformation and contact force, it can be inferred that the PRCs also provide an understanding of the system's response to the transient.

7. Conclusions

In this paper, the dynamic response of a single-degree-of-freedom Vibro-Impact Isolation System subjected to harmonic actions is studied through parametric numerical analyses. This new, strongly nonlinear system is defined by coupling an initial, linearly isolated system with bumpers, arranged symmetrically with respect to the initial system, with an appropriate initial gap, and suitably designed. Therefore, the responses of different scenarios obtained by varying the gap parameter δ_0, which is related through the optimal curve (Fig. 6a) and the optimality relationship (Eq.(7)) to the other two parameters governing the impact (damping γ and stiffness λ of the bumpers), both at steady-state and transient state, are analyzed. This study aims to solve the problems of linear isolated systems (large dynamic and static displacements and high response values when the system is in the resonance range), but without losing the benefits of linear isolated systems. The response quantities selected are absolute acceleration and relative

displacement of the mass, and contact force and deformation of the bumpers, also highlighting the response of static displacement.

Based on the different responses, the following conclusion can be formed:

- Comparing the curves representing the absolute maximum values of steady-state response, both of displacement and of acceleration, as a function of frequency ratio (PRCs), obtained in the free-flight condition (FF) with those obtained at the occurrence of impact, it can be seen that the V-IISs intervene on the response selectively, introducing additional viscous damping in a limited range of β, between $\beta_1(\delta_0)$ and $\beta_2(\delta_0)$, for each δ_0. If $\delta_0 \geq \delta_{0c}$, the only positive effects of energy dissipation in the non-isolation range are obtained: greater reductions in response, with respect to FF, of both displacement and acceleration, as δ_0 decreases, without obtaining increases in response in the isolation range. In fact, for the cases in which the V-IIS was designed with a $\delta_0 = 0.3$ and $\delta_0 = 0.19$, a reduction in dynamic amplification of 21% and 31%, respectively, in terms of acceleration, and 42% and 56%, respectively, in terms of displacement was obtained compared with the linear system; this was precisely without obtaining an increase in the β of isolation onset $\beta_c(\delta_0)$. When $\delta_0 < \delta_{0c}$, on the other hand, even though we continue to have increasing reductions in maximum response values as the gap decreases, with respect to FF, we begin to have a reduction in the isolation range, resulting in increases in response, with respect to FF, for β between $\sqrt{2}$ and the value $\beta_2(\delta_0)$, representative of the frequency ratio beyond which there is no longer impact for a fixed value of δ_0. In fact, for the cases in which the V-IIS was designed with a $\delta_0 = 0.03$ and $\delta_0 = 0$, a reduction in dynamic amplification of 54% and 62%, respectively, in terms of acceleration, and 82% and 90%, respectively, in terms of displacement was obtained compared with the linear system, while reporting an increase in $\beta_2(\delta_0)$ that turns out to be 2.8 for $\delta_0 = 0.03$ and tends to infinity for $\delta_0 = 0$. Therefore, for $\beta_c(\delta_0) \langle \beta > \beta_2(\delta_0)$ the V-IIS reports greater responses than the linear case.
- From the PRCs of displacement, the benefits that V-IIS can bring on static displacement are observed: when $\delta_0 \geq \delta_0^*$ ($\delta_0^* \simeq \delta_{0c}$), static displacement is unchanged with respect to FF ($q_{st} \simeq 0.19$); choosing $\delta_0 < \delta_0^*$, however, there is a greater reduction in q_{st} as δ_0 decreases, assuming the minimum value at $\delta_0 = 0$, which is $q_{st} \simeq 0.08$. In addition, to highlight the dependence of the static displacement on the isolation frequency β_I with which the system is designed, which does not emerge by normalizing the displacement with respect to the maximum displacement in resonance, a new dimensionless parameter representing the static displacement is introduced, in which the dimensional static displacement is normalized with respect to the peak ground displacement. It can thus be seen that the static displacement increases as β_I increases, and that this trend is attenuated more and more as δ_0 decreases. The static displacement q_{st}^*, for δ_0 equal to 0.3 and 0.19 ($\delta_0 \geq \delta_0^*$), turns out to be the same as in the FF; whereas, for δ_0 equal to 0.03 and 0 ($\delta_0 < \delta_0^*$), it undergoes a reduction of 44% and 61%, respectively.
- Comparing PRCs in both contact force and bumper deformation, we observe the maximum values of these quantities in the resonance range, where acceleration and displacement show the greatest reductions compared with FF: the contact force takes on a nearly equal value for all δ_0 equal to 0.3, while the strain turns out to be, for $\delta_0 = 0.3, 0.28$,for $\delta_0 = 0.19, 0.25$, for $\delta_0 = 0.03, 0.15$ and, for $\delta_0 = 0, 0.10$. In the frequency range following resonance, both contact force and bumper deformation show modest values.
- Through the time histories of the investigated quantities, obtained by applying a harmonic excitation of varying frequency, the transient response of the V-IISs can be studied: during the ramping up of the frequency of the harmonic excitation, the system also assumes the β values close to resonance, so the impact with the optimally designed bumpers allows an effective control of the system response. Another important result that these investigations have yielded is that PRCs, obtained with sweeps performed by applying the continuation technique, (which show the maximum values at steady-state) reproduce an envelope of the maximum values of the reference quantity reported in the time histories.

These conclusions allow us to state that the optimal design of V-IISs is achieved through the choice of δ_0 such that $\beta_2(\delta_0)$ values (frequency ratio beyond which impact no longer occurs for that δ_0) are lower than the isolation frequency β_I of the system. This introduces selective damping β that can reduce the system responses in the resonance range and limits the static displacement; while for values of β equal to β_I, (isolation frequency ratio with which it was designed) the system behaves as a linear isolated system, showing the lowest values of absolute acceleration response with values of frequency ratio β in the isolation range.

The aim of this study is to define a new strategy for controlling the dynamic response of structures and equipment, both for the presence of vibrating machines and for seismic actions of particular magnitude. In the case of seismic actions at the base, the assumption of representing such multi-frequency actions with the effective fundamental frequency of vibration of the structure can be an effective solution to represent the response of the structure. Therefore, the effectiveness of these hybrid systems subjected to seismic actions and in the case of continuous systems that can be assimilated to multi-degree-of-freedom systems will have to be investigated further, both through further parametric numerical investigations and experimental investigations.

Declaration of Competing Interest

The authors declare that they have no known competing financial interests or personal relationships that could have appeared to influence the work reported in this paper.

Acknowledgments

This work was partially funded by Sapienza University of Rome [grant numbers RM120172B8FDDB0C]

Appendix A. Supplementary data

Supplementary data to this article can be found online at https://doi.org/10.1016/j.istruc.2023.105270.

References

[1] Jangid RS, Kelly JM. Base isolation for near-fault motions. Earthq Eng Struct Dyn 2001;30(5):691–707. https://doi.org/10.1002/eqe.31.
[2] Dicleli M, Buddaram S. Equivalent linear analysis of seismic-isolated bridges subjected to near-fault ground motions with forward rupture directivity effect. Eng Struct Jan. 2007;29(1):21–32. https://doi.org/10.1016/j.engstruct.2006.04.004.
[3] Crozet V, Politopoulos I, Yang M, Martinez J, Erlicher S. Sensitivity analysis of pounding pounding between adjacent structures. Earthq Eng Struct Dyn 2018;47 (1):219–35. https://doi.org/10.1002/eqe.2949ï.
[4] Komodromos P, Polycarpou PC, Papaloizou L, Phocas MC. Response of seismically isolated buildings considering poundings. Earthq Eng Struct Dyn Oct. 2007;36(12): 1605–22. https://doi.org/10.1002/eqe.692.
[5] Polycarpou PC, Komodromos P. On poundings of a seismically isolated building with adjacent structures during strong earthquakes. Earthq Eng Struct Dyn 2010;39 (8):933–40. https://doi.org/10.1002/eqe.975.
[6] Pant DR, Wijeyewickrema AC. Performance of base-isolated reinforced concrete buildings under bidirectional seismic excitation considering pounding with retaining walls including friction effects. Earthq Eng Struct Dyn 2014;43(10): 1521–41. https://doi.org/10.1002/eqe.2409.
[7] Meng D, Yang M, Yang Z, Chouw N. Effect of earthquake-induced transverse poundings on a 32 m span railway bridge isolated by friction pendulum bearings. Eng Struct Jan. 2022;251. https://doi.org/10.1016/j.engstruct.2021.113538.
[8] Reggio A, De Angelis M. Optimal design of an equipment isolation system with nonlinear hysteretic behaviour. Earthq Eng Struct Dyn Oct. 2013;42(13):1907–30. https://doi.org/10.1002/eqe.2304.

[9] Reggio A, De Angelis M. Combined primary-secondary system approach to the design of an equipment isolation system with High-Damping Rubber Bearings. J Sound Vib Apr. 2014;333(9):2386–403. https://doi.org/10.1016/j.jsv.2013.12.006.
[10] Yu C, Fu Q, Zhang J, Zhang N. The vibration isolation characteristics of torsion bar spring with negative stiffness structure. Mech Syst Sig Process 2022;180:109378.
[11] Zeng R, Yin S, Wen G, Zhou J. A non-smooth quasi-zero-stiffness isolator with displacement constraints. Int J Mech Sci 2022;225:107351.
[12] Wang X, Liu H, Chen Y, Gao P. Beneficial stiffness design of a high-static-low-dynamic-stiffness vibration isolator based on static and dynamic analysis. Int J Mech Sci Jul. 2018;142–143:235–44. https://doi.org/10.1016/j.ijmecsci.2018.04.053.
[13] Carrella A, Brennan MJ, Waters TP, Lopes V. Force and displacement transmissibility of a nonlinear isolator with high-static-low-dynamic-stiffness. Int J Mech Sci Feb. 2012;55(1):22–9. https://doi.org/10.1016/j.ijmecsci.2011.11.012.
[14] Renzi E, De Angelis M. Optimal semi-active control and non-linear dynamic response of variable stiffness structures. J Vib Control Oct. 2005;11(10):1253–89. https://doi.org/10.1177/1077546305054597.
[15] Du H, Han M, Wang H, Wang Y, Jiang J, Yu J. Impact model and computational analysis of structural isolation layer deformation limitation with limiters. Structures Jun. 2022;40:176–86. https://doi.org/10.1016/j.istruc.2022.03.085.
[16] Du H, Wang Y, Han M, Ibarra LF. Experimental seismic performance of a base-isolated building with displacement limiters. Eng Struct 2021;244:112811.
[17] Polycarpou PC, Komodromos P, Polycarpou AC. A nonlinear impact model for simulating the use of rubber shock absorbers for mitigating the effects of structural pounding during earthquakes. Earthq Eng Struct Dyn 2013;42(1):81–100. https://doi.org/10.1002/eqe.2194.
[18] Andreaus U, De Angelis M. Nonlinear dynamic response of a base-excited SDOF oscillator with double-side unilateral constraints. Nonlinear Dyn May 2016;84(3):1447–67. https://doi.org/10.1007/s11071-015-2581-4.
[19] Andreaus U, Baragatti P, De Angelis M, Perno S. A Preliminary Experimental Study about Two-Sided Impacting SDOF Oscillator under Harmonic Excitation. J Comput Nonlinear Dyn 2017;12(6):Nov. https://doi.org/10.1115/1.4036816.
[20] Andreaus U, Baragatti P, De Angelis M, Perno S. Shaking table tests and numerical investigation of two-sided damping constraint for end-stop impact protection. Nonlinear Dyn Dec. 2017;90(4):2387–421. https://doi.org/10.1007/s11071-017-3810-9.
[21] Andreaus U, De Angelis M. Experimental and numerical dynamic response of a SDOF vibro-impact system with double gaps and bumpers under harmonic excitation. Int J Dyn Control Dec. 2019;7(4):1278–92. https://doi.org/10.1007/s40435-019-00532-x.
[22] Andreaus U, De Angelis M. Influence of the characteristics of isolation and mitigation devices on the response of single-degree-of-freedom vibro-impact systems with two-sided bumpers and gaps via shaking table tests. Struct Control Health Monit 2020;27(5).
[23] Stefani G, De Angelis M, Andreaus U. Scenarios in the experimental response of a vibro-impact single-degree-of-freedom system and numerical simulations. Nonlinear Dyn Mar. 2021;103(4):3465–88. https://doi.org/10.1007/s11071-020-05791-4.
[24] Stefani G, De Angelis M, Andreaus U. Numerical study on the response scenarios in a vibro-impact single-degree-of-freedom oscillator with two unilateral dissipative and deformable constraints. Commun Nonlinear Sci Numer Simul 2021;99:105818.
[25] Stefani G, De Angelis M, Andreaus U. Influence of the gap size on the response of a single-degree-of-freedom vibro-impact system with two-sided constraints: Experimental tests and numerical modeling. Int J Mech Sci 2021;206:106617.
[26] Stefani G, De Angelis M, Andreaus U. The effect of the presence of obstacles on the dynamic response of single-degree-of-freedom systems: Study of the scenarios aimed at vibration control. J Sound Vib 2022;531:116949.
[27] Chopra AK. Dynamics of Structures: Theory and Applications to Earthquake Engineering. Pearson, Englewood Cliffs: New Jersey, fourth edn; 2012.